Publ. Astron. Soc. Japan (2022) 00(0), 1–28
doi: 10.1093/pasj/xxx000

A 16 deg^2 survey of emission-line galaxies at z$<$1.5 in HSC-SSP PDR1

Masao HAYASHI[1], Masayuki TANAKA[1], Rhythm SHIMAKAWA[1,2], Hisanori FURUSAWA[1], Rieko MOMOSE[3], Yusei KOYAMA[4,5], John D. SILVERMAN[6], Tadayuki KODAMA[1,5,7], Yutaka KOMIYAMA[1,5], Alexie LEAUTHAUD[8], Yen-Ting LIN[9], Satoshi MIYAZAKI[1,5], Tohru NAGAO[10], Atsushi J. NISHIZAWA[11], Masami OUCHI[6,12], Takatoshi SHIBUYA[12], Ken-ichi TADAKI[1,13] and Kiyoto YABE[6]

[1]National Astronomical Observatory of Japan, 2-21-1 Osawa, Mitaka, Tokyo 181-8588, Japan
[2]UCO/Lick Observatory, University of California, 1156 High Street, Santa Cruz, CA 95064, USA
[3]Institute of Astronomy, National Tsing Hua University, 101, Section 2 Kuang-Fu Road, Hsinchu, Taiwan, 30013, R.O.C.
[4]Subaru Telescope, National Astronomical Observatory of Japan, 650 N Aohoku Pl, Hilo, HI 96720
[5]Department of Astronomy, School of Science, Graduate University for Advanced Studies (SOKENDAI), 2-21-1, Osawa, Mitaka,Tokyo 181-8588, Japan
[6]Kavli Institute for the Physics and Mathematics of the Universe (Kavli IPMU, WPI), The University of Tokyo, 5-1-5 Kashiwanoha, Kashiwa, Chiba, 277-8583, Japan
[7]Astronomical Institute, Tohoku University, Aramaki, Aoba-ku, Sendai 980-8578, Japan
[8]Department of Astronomy and Astrophysics, University of California, Santa Cruz, 1156 High Street, Santa Cruz, CA 95064 USA
[9]Academia Sinica Institute of Astronomy and Astrophysics, P.O. Box 23-141, Taipei 10617, Taiwan
[10]Research Center for Space and Cosmic Evolution, Ehime University, 2-5 Bunkyo-cho, Matsuyama, Ehime 790-8577, Japan
[11]Institute for Advanced Research, Nagoya University, Chikusaku, Nagoya 464-8602, Japan
[12]Institute for Cosmic Ray Research, The University of Tokyo, 5-1-5 Kashiwanoha, Kashiwa, Chiba 277-8582, Japan
[13]Max-Planck-Institut für Extraterrestrische Physik, Giessenbachstrasse, D-85748 Garching, Germany

*E-mail: masao.hayashi@nao.ac.jp

Received ; Accepted

Abstract

We present initial results from the Subaru Strategic Program (SSP) with Hyper Suprime-Cam (HSC) on a comprehensive survey of emission-line galaxies at $z < 1.5$ based on narrowband imaging. The first Public Data Release (PDR1) provides us with data from two narrowband filters, specifically NB816 and NB921 over 5.7 deg^2 and 16.2 deg^2 respectively. The 5σ limiting magnitudes are 25.2 (UltraDeep layer, 1.4 deg^2) and 24.8 (Deep layer, 4.3 deg^2) mag in NB816, and 25.1 (UltraDeep, 2.9 deg^2) and 24.6–24.8 (Deep, 13.3 deg^2) mag in NB921. The wide-field imaging allows us to construct unprecedentedly large samples of 8,054 Hα emitters

at $z \approx 0.25$ and 0.40, 8,656 [OIII] emitters at $z \approx 0.63$ and 0.84, and 16,877 [OII] emitters at $z \approx 1.19$ and 1.47. We map the cosmic web on scales out to about 50 comoving Mpc that includes galaxy clusters, identified by red sequence galaxies, located at the intersection of filamentary structures of star-forming galaxies. The luminosity functions of emission-line galaxies are measured with precision and consistent with published studies. The wide field coverage of the data enables us to measure the luminosity functions up to brighter luminosities than previous studies. The comparison of the luminosity functions between the different HSC-SSP fields suggests that a survey volume of $> 5 \times 10^5$ Mpc^3 is essential to overcome cosmic variance. Since the current data have not reached the full depth expected for the HSC-SSP, the color cut in $i-$NB816 or $z-$NB921 induces a bias towards star-forming galaxies with large equivalent widths, primarily seen in the stellar mass functions for the Hα emitters at $z \approx 0.25$–0.40. Even so, the emission-line galaxies clearly cover a wide range of luminosity, stellar mass, and environment, thus demonstrating the usefulness of the narrowband data from the HSC-SSP to investigate star-forming galaxies at $z < 1.5$.

Key words: galaxies: evolution — galaxies: high-redshift — galaxies: luminosity function, mass function — large-scale structure of universe

1 Introduction

Emission lines from HII regions in galaxies are one of the important spectral features to characterize galaxies. The intensity of the nebular emission in the rest-frame optical wavelength such as Hα ($\lambda = 6565$Å in a vacuum), [OIII] ($\lambda\lambda = 4960, 5008$Å), H$\beta$ ($\lambda = 4863$Å) and [OII] ($\lambda\lambda = 3727, 3730$Å) is sensitive to star formation rate (SFR) of galaxies and thus widely used as an indicator of SFR of galaxies (e.g., Kennicutt 1998; Moustakas et al. 2006). While the luminosity of hydrogen lines such as Hα and Hβ is directly linked to the number of ionizing photons, the physics associated with the emission lines from oxygen, caused by collisional excitation, are more complicated than those from hydrogen and depend on the physical condition of the nebular gas such as metallicity and ionization state. However, it is known that the intensity of emission lines from ionized oxygen, especially from [OII], is a usable indicator of SFR in galaxies not only in the local Universe but also at high redshifts (e.g., Kennicutt 1998; Kewley et al. 2004; Moustakas et al. 2006; Hayashi et al. 2013; Hayashi et al. 2015). Recent studies also demonstrate that typical star forming galaxies at high redshifts, especially $z > 2$–3, are often identified as [OIII] emission-line galaxies (Ly et al. 2007; Drake et al. 2013; Khostovan et al. 2015; Suzuki et al. 2016). Therefore, emission lines are a useful tool to sample and investigate star-forming galaxies at various redshifts.

Many surveys, targeting emission-line galaxies at $z \lesssim 2$, have been conducted so far (e.g., Bunker et al. 1995; Thompson et al. 1996; Moorwood et al. 2000; van der Werf et al. 2000; Fujita et al. 2003; Doherty et al. 2006; Shioya et al. 2008; Villar et al. 2008; Dale et al. 2010; Ly et al. 2007; Ly et al. 2011; Bayliss et al. 2011; Lee et al. 2012; Best et al. 2013; Colbert et al. 2013; Ciardullo et al. 2013; Drake et al. 2013; Pirzkal et al. 2013; Sobral et al. 2013; Sobral et al. 2015; An et al. 2014; Khostovan et al. 2015; Comparat et al. 2015; Comparat et al. 2016; Stroe & Sobral 2015; Stroe et al. 2017). As a result, the cosmic SFR density has been established with a peak at $z = 1$–3 and then a gradually decline towards the local Universe (e.g., Hopkins & Beacom 2006; Madau & Dickinson 2014). Star-forming galaxies at each redshift show a tight correlation between SFR and stellar mass irrespective of environment where galaxies are located, which is called a main sequence of star-forming galaxies (e.g., Daddi et al. 2007; Elbaz et al. 2007; Noeske et al. 2007; Koyama et al. 2013; Koyama et al. 2014; Suzuki et al. 2016; Hayashi et al. 2016; Ramraj et al. 2017; Oteo et al. 2015; Sobral et al. 2014; Kashino et al. 2013; Shivaei et al. 2015), and star-forming galaxies at a fixed stellar mass have smaller SFRs at lower redshifts (e.g., Speagle et al. 2014; Whitaker et al. 2014; Tomczak et al. 2016). The main sequence of star-forming galaxies indicates that only a few percent of galaxies are in a starburst phase (Rodighiero et al. 2011). The fact that few galaxies are outliers from the main sequence is considered to be an evidence that a time scale of starburst phase and quenching of star formation is short. However, physics governing the evolution of individual galaxies is not yet well understood. What triggers the starburst in galaxies? What quenches the star formation of galaxies? How have galaxies evolved along large-scale structures of the cosmic web? As a first step to address these important issues for understanding galaxy evolution, a more comprehensive sampling of star-forming galaxies at the redshifts of $z \lesssim 3$ is required that covers a wide range in terms of star formation activity and environment. Recent studies have indeed demonstrated the importance of investigating galaxy properties along the cosmic web (e.g., Darvish et al. 2014; Darvish et al. 2015; Darvish et al.

2016; Darvish et al. 2017; Malavasi et al. 2017; Laigle et al. 2017; Kuutma et al. 2017).

Surveys of emission-line galaxies are basically performed with either spectroscopy or narrowband (NB) imaging. Spectroscopic surveys have the advantage of identifying emission lines and measuring line luminosities. However, target selection for spectroscopy can cause biases with the observed galaxy sample. Rather than slit or fiber spectroscopy, an integral field unit spectrograph such as VLT/MUSE (Bacon et al. 2015; Meillier et al. 2016; Bina et al. 2016; Swinbank et al. 2017) or grism such as HST/WFC3 (e.g., Atek et al. 2010; van Dokkum et al. 2011; Straughn et al. 2011; van der Wel et al. 2011; Brammer et al. 2012; Colbert et al. 2013; Pirzkal et al. 2013; Mehta et al. 2015; Morris et al. 2015; Momcheva et al. 2016) can overcome selection biases by allowing us to get spectrum of all galaxies over the field surveyed. One weakness is the small field of view (FoV). Alternatively, NB imaging surveys of emission-line galaxies allow us to cover a wide, homogeneous FoV without any bias for target selection. Although, the selection with NB imaging requires an equivalent width (EW) of emission lines larger than a certain limit, thus sampling strong nebular emission lines. As a result, this approach is able to effectively produce comprehensive samples of star-forming galaxies.

Indeed, previous studies with NBs (e.g., Ly et al. 2007; Drake et al. 2013; Sobral et al. 2011; Sobral et al. 2013; Sobral et al. 2015; Khostovan et al. 2015; Matthee et al. 2017) have succeeded in constructing large samples of emission-line galaxies at $z < 2$. Ly et al. (2007) have selected 200-900 emission-line galaxies with 11 individual redshift slices at $z < 1.5$ from deep imaging with 4 NB filters in 0.24 deg^2 of the Subaru Deep Field (SDF). Drake et al. (2013) have presented catalogs of more than 5000 emission-line galaxies at $z \lesssim 1.6$ from a survey with 6 NB filters in 0.63 deg^2 of the Subaru/XMM-Newton Deep Survey (SXDS) field. Samples of emission-line galaxies of similar size at $z \lesssim 2$ are also presented by the High-redshift(Z) Emission Line Survey (HiZELS). Sobral et al. (2013) have conducted deep surveys in ~ 2.0 deg^2 of the COSMOS and SXDS fields, while Sobral et al. (2015) have conducted shallower but wider surveys in ~ 10 deg^2 of the SA22 fields. They map large-scale structures of Hα emitters over these fields (see also Sobral et al. 2011).

Here, we use Hyper Suprime-Cam (HSC), an instrument on the Subaru Telescope capable of delivering good image quality over a FoV of 1.77 deg^2 in a single pointing (Miyazaki et al. 2012; Miyazaki et al. 2017). The Subaru Strategic Program (SSP) with HSC is a three-layered (Wide, Deep (D), and UltraDeep (UD)), multi-band (five broadband (BB) filters: $grizy$ plus four NB filters: NB387, NB816, NB921, and NB101, Figure 1) imaging survey (Aihara et al. 2017b). The survey started in March 2014 and is ongoing. The HSC-SSP

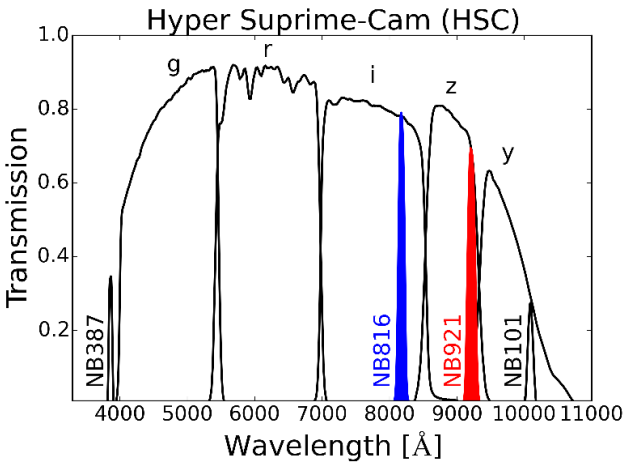

Fig. 1. The set of broadband (BB) and narrowband (NB) filters used in the HSC-SSP. Among the four NB filters, the data in two NB filters, NB816 (blue) and NB921 (red), are available with the PDR1 data (Table1). The response function of the filters and the quantum efficiency of CCD are taken into account for the transmission. The specification of the NB is shown in Table 2.

program will be conducted in 300 nights spread over 5–6 years. The observations with the NB filters are conducted in the UD and D fields. When the program is completed, the NB921 data will reach down to 26.5 (25.9) mag and the z-band data down to 27.1 (26.6) mag over 3.5 (26) deg^2 of the UD (D) fields (Aihara et al. 2017b). The set of four NB filters installed in HSC enables us to select not only Lyman α emitters at $z \sim 2.2$, 5.7, 6.7, and 7.3, but also galaxies with nebular emission such as Hα, [OIII]($\lambda\lambda = 4960, 5008$Å), and [OII]($\lambda\lambda = 3727, 3730$Å) at $z \lesssim 1.7$. Undoubtedly, the HSC-SSP survey provides us with one of the most comprehensive samples of line-emitting galaxies which are useful to study the evolution of galaxies at low and intermediate redshifts. Therefore, the goal of this paper is to construct catalogs of the emission-line galaxies from the HSC-SSP PDR1 data and then investigate basic global properties of the selected galaxies.

The outline of this paper is as follows. In § 2, the NB data from HSC-SSP are described and the quality is verified. In § 3, emission-line galaxies at $z = 0.25$–1.47 are selected and then catalogs of the galaxies are created. In § 4, the spatial distribution and luminosity functions are constructed. In § 5, we discuss cosmic variance, the bright end of the luminosity function while taking advantage of the wide field data. We also investigate the stellar mass function for the emission-line galaxies to better understand the samples of emission-line galaxies. Finally, our conclusions are presented in § 6. Throughout this paper, a composite model magnitude named `cmodel` is used for the photometry of galaxies and magnitudes are presented in the AB system (Oke & Gunn 1983), unless otherwise mentioned. The `cmodel` photometry measures fluxes of objects by simultaneously fitting two components of a de Vaucouleur and an exponential profile

Table 1. Narrowband data available in HSC-SSP PDR1.

Field*	Narrowband filter					
	NB816			NB921		
	Area† [deg^2]	Integration [hour]	Limit mag.‡	Area† [deg^2]	Integration [hour]	Limit mag.‡
UD-COSMOS	···	···	···	1.47 (1.54)	7.0	25.1
UD-SXDS	1.43	4.0	25.2	1.49	4.8	25.1
D-COSMOS	···	···	···	2.27 (2.91)	2.0	24.8
D-DEEP2-3	4.25	1.0	24.8	5.63	1.0	24.6
D-ELAIS-N1	···	···	···	5.37	1.0	24.6
total area	5.68			16.2		

* The coordinates of fiducial pointing in each field are defined in the survey design paper of Aihara et al. (2017b).

† An effective area, i.e., the masked regions are excluded. The value in the parenthesis shows the effective area including the overlapping regions (0.72 deg^2) between the UD-COSMOS and D-COSMOS fields.

‡ A median value of 5σ limiting magnitudes in the individual `patch`[1] regions, which are estimated from the standard deviation of sky values measured with randomly-distributed $2''$ diameter apertures.

Table 2. Narrowband filters.

	λ_c † [Å]	$\Delta\lambda$ † [Å]	Hα ($\lambda = 6564.6$)‡		[OIII] ($\lambda = 5008.2$)‡		[OII] ($\lambda = 3727.1, 3729.9$)‡	
			z	z range	z	z range	z	z range
NB816	8177	113	0.246	0.237 – 0.254	0.633	0.621 – 0.644	1.19	1.18 – 1.21
NB921	9214	135	0.404	0.393 – 0.414	0.840	0.826 – 0.853	1.47	1.45 – 1.49

† The value is derived from the area-weighted mean response function (Kawanomoto et al. 2017, in prep.).

‡ Vacuum wavelength in the rest-frame in units of Å.

convolved with point spread function (PSF) (see Bosch et al. 2017 for the details). The cosmological parameters of $H_0 = 70$ km s^{-1} Mpc^{-1}, $\Omega_m = 0.3$ and $\Omega_\Lambda = 0.7$, along with Chabrier (2003) initial mass function (IMF), are adopted.

2 DATA

2.1 HSC-SSP PDR1

This work is based on the first Public Data Release (PDR1) of the HSC-SSP which were available on 2017 February 28 (Aihara et al. 2017a). The processing of the HSC-SSP data, including data reduction, object detection, and photometry, is conducted with the HSC software pipeline (hscPipe 4.0.1, Bosch et al. 2017), essentially equivalent to that for the Large Synoptic Survey Telescope (LSST, Ivezic et al. 2008; Axelrod et al. 2010; Jurić et al. 2015). The astrometry and photometry are calibrated with Pan-STARRS1 (PS1, Tonry et al. 2012; Schlafly et al. 2012; Magnier et al. 2013). One should refer to Aihara et al. (2017a) for full details regarding the data set of the HSC-SSP PDR1 and to Bosch et al. (2017) for the data processing. Hereafter, we briefly describe critical points with respect to the data products including the photometry.

In this release, NB data from two filters (NB816 and NB921; Table 1) are available. Of the two UD fields and four D fields defined in the HSC-SSP survey, the NB816 data are taken in one UD field and one D field, while the NB921 data are taken in both UD fields and three D fields, which results in an effective coverage of 5.68 (16.2) deg^2 by 4 (12) FoVs of HSC using NB816 (NB921). Since the NB921 data have an 0.72 deg^2 of overlap between the UD-COSMOS and D-COSMOS fields, we account for this when determining the total effective area coverage. The median seeing is 0.62 (0.70) arcsec in NB816 (NB921), respectively. The integration time of the NB data are 4-7 hours in the UD fields and 1-2 hours in the D fields. The 5σ limiting magnitudes of NB816 are 25.2 and 24.8 in the UD and D fields, and those of NB921 are 25.1 and 24.6 in the UD and D fields. The limiting magnitudes provided here are estimated from the standard deviation of sky values within randomly-distributed $2''$ diameter apertures. Note that Aihara et al. (2017a) measure the 5σ depth for point sources in a different manner. The data from all of the five BBs, $grizy$, are also available in the area covered by the NB data. The median seeing ranges from 0.61 – 0.83 arcsec. The i and z-band data are > 0.5 mag deeper than the NB816 and NB921 data, thus indicating a depth sufficient for the selection of emission-line galaxies.

hscPipe conducts photometry in two ways for all individual sources detected in any of the available bands. One is `unforced` photometry that is conducted in each band separately, while the other is `forced` photometry that is conducted in each band on a fixed position with the fixed profile of objects determined in a single reference band. The reference band for the `forced` photometry is selected according to the priority order of i, r, z, y, g, NB921 and NB816 for the individual objects based on which band and at what signal-to-noise ratio (SNR) the objects are detected. For instance, even if an object is detected in NB, as long as it has a detection in any of BBs at high enough SNR, the BB (most likely i-band) is selected as a reference band for the `forced` photometry.

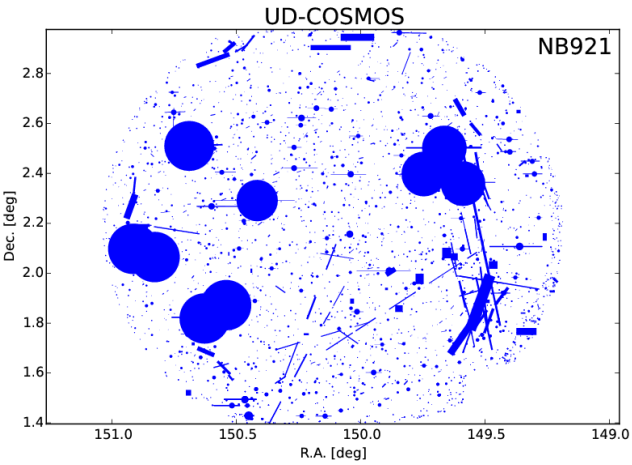

Fig. 2. The mask regions for NB921 data in the UD-COSMOS field are shown in blue, which are used to exclude satellite trails, moving objects, and ghost-like features in the coadded NB images.

2.2 Catalogs of galaxies detected in narrowbands

Catalogs of objects are retrieved from the Catalog Archive Server (CAS) of the HSC-SSP data (Takata et al. 2017, in prep.). We describe how to select the NB-detected galaxies in this section, and the details of the flags we apply are shown in Appendix 1.

2.2.1 NB-detected objects

Detection in any of the NB filters is a necessary condition, because we are interested in galaxies with a nebular emission line that enters NB816 or NB921. We select deblended objects that are detected in NB816 or NB921 at a SNR, `flux_cmodel/flux_cmodel_err`, greater than 5 in the `unforced` photometry. We also require that the objects meet the criteria for a likely significant detection of the `cmodel` measurement in a region that is not affected by saturation, cosmic rays, and bad pixels. Since the edge regions where the number of co-added frames in NB816 or NB921 is less than 3 (10) in the D (UD) fields are shallower than the other regions of the D (UD) fields, objects in the shallow regions are removed. With these requirements, we generate catalogs of NB-detected objects with clean photometry from the catalog database. However, we notice that there can be satellite trails, moving objects, and ghost-like features left in the coadded NB images, which are the known problems in the HSC-SSP PDR1 (Aihara et al. 2017a). Some regions around very bright stars and near the edge of the FoV also have bad quality. Therefore, we apply masks to exclude such objects and regions from the catalogs. While hscPipe already provides bright object masks and flags for masking (Coupon et al. 2017), the masks that we produce as described in the next section are complementary to those provided by the HSC-SSP.

2.2.2 Masked regions

Because a single `visit`[1] with the NB filter is taken with a long exposure time (15 min), satellite trails are seen in NB images. Note that the bright satellite trails are removed from the `coadd` image by combining the `visit` images while clipping pixels having significantly deviant fluxes. If there are satellite trails and moving objects only in the NB images, such objects can be regarded as objects that are much brighter in NB than in BB and then misidentified as emission-line galaxies. Therefore, it is important to exclude such objects by masking them.

To find the satellite trails and moving objects in the `coadd` NB image, the individual warped `visit` images are examined. Among pixels with a detection flag on in the mask layer stored in the `coadd` fits image, we search for pixels that attribute the detection to a large flux from only a single `visit` image. Pixels forming a line on the `coadd` image are candidates of satellite trails and moving objects. We set the mask regions to cover the pixels of satellite trails and moving objects. We then make fine adjustments to the masks manually. We also add additional mask regions for the bleed trails of saturated stars based on the mask image layer of the `coadd` fits image.

Figure 2 shows the mask regions for NB921 data in the UD-COSMOS field. The masks for NB816 and NB921 data are available in all of the other fields as well. The effective area shown in Table 1 is an area of the unmasked region that is calculated with the `random` catalog including the randomly distributed objects (Aihara et al. 2017a).

2.2.3 Removal of stars and junk objects

Furthermore, we need to exclude stellar objects as well as junk objects that hscPipe cannot identify. In order to exclude stars, we use a probability of an object being a star, `pstar`, which is estimated by a supervised learning star/galaxy classification code (Bosch et al. 2017). The information of `pstar` is available in the S15B internal release but not in the HSC-SSP PDR1 data as of the public release in 2017 February. Note that in the UD and D fields the S15B internal release data are equivalent to the PDR1 data (Aihara et al. 2017a). We also use the flag of `classification_extendedness`, which can identify stellar objects with few contaminants down to $i \sim 23$ (Aihara et al. 2017a). We find that the two flags are complementary and the combination of `pstar` and `classification_extendedness` is more effective at identifying stellar objects. Objects with the flag of `pstar`>0.5 or `classification_extendedness`$=0 \wedge$ `mag_psf`<23.0 in i-band are rejected as stellar objects, which amounts to $\sim$7-13% of the NB-detected objects in each field. This procedure can exclude not only stars but also point sources such as active galactic nuclei (AGNs), which is discussed in

[1] The followings are HSC/LSST-specific terms seen in this paper (Aihara et al. 2017a). `visit` is an ID number of the individual shots. `tract` is a pre-defined region covering $\sim 1.7 \times 1.7$ deg^2. A single `tract` is divided into 9×9 sub-regions called `patch` that covers $\sim 12 \times 12$ arcmin^2.

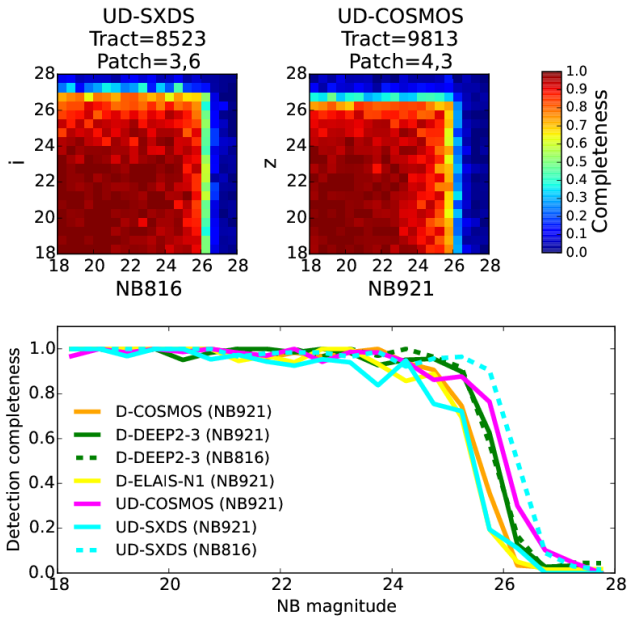

Fig. 3. Detection completeness as a function of i (z) and NB816 (NB921) magnitudes. The upper left panel shows the completeness for NB816-detected objects in the UD-SXDS field, while the upper right panel shows for NB921-detected objects in the UD-COSMOS field. Synthetic objects with a profile of the PSF and various combination of i and NB816 magnitudes (or z and NB921) are randomly embedded within images to measure the completeness. The lower panel shows the detection completeness in NBs for the individual fields as a function of NB magnitude.

§ 3.5. We find that large objects with a minor axis greater than 3 arcsec or small objects with a major axis less than the size of PSF are highly likely to be flagged as a junk object. These objects are also removed from the catalogs.

2.3 Quality verification of NB data

2.3.1 Detection completeness

Detection completeness is important to determine the faint end of number counts (§ 2.3.3) and luminosity functions (§ 4.2). To assess the completeness for individual fields, we use the software pipeline, SynPipe (Huang et al. 2017), which can randomly embed artificial objects in the individual CCD images. Then, we run hscPipe on the CCD images with the synthetic objects to conduct the same processes of coadd, object detection, and photometry as for the original data. We compare the catalog of detected sources output by hscPipe with the list of synthetic objects input to SynPipe, where we use an aperture with a radius of 2 pixels (i.e., 0.34 arcsec) for matching between the input and output catalogs without any constraint on magnitude difference. Since emission-line galaxies are selected based on a color of NB and BB both of which cover the same wavelengths, the completeness of emission-line galaxies should depend on the color of $i-$NB816 ($z-$NB921) for NB816 (NB921) emitters. Therefore, we investigate the completeness as a function of i (z) and NB816 (NB921) as shown in Figure 3.

We construct objects with a profile of the PSF as synthetic objects for the measurement of detection completeness. The PSF is modeled on each CCD image by hscPipe based on the actual stars (refer to Bosch et al. 2017 for the details of the PSF modeling). We note that galaxies do not have a profile of the PSF but rather have an extended profile. However, star-forming galaxies at $z < 2$ have varying profiles depending on their intrinsic properties thus it is reasonable to assume such a simplification of the profile of synthetic objects. Our assumption of the PSF profile can result in the overestimate of the detection completeness.

To investigate the completeness of objects with a given i or z magnitude, we make an input list of 1,000 synthetic objects with NB816 or NB921 of 18.0–28.0 mag at 0.5 mag bin of BB in each `patch`. Then, twenty input lists are prepared to cover the same range of BB magnitudes as the NB magnitudes (18.0–28.0 mag). In this procedure, we run SynPipe in a single `patch` in each field per each NB data. We select the following representative `patch`, where there are not any very bright stars, satellite trails, and bad areas, for each field: (`tract`[1], `patch`) = (9813, '7,7') for D-COSMOS, (9706, '1,3') for D-DEEP2-3, (17130, '3,2') for D-ELAIS-N1, (9813, '4,3') for UD-COSMOS, (8523, '3,6') for UD-SXDS. The detection completeness estimated in UD-SXDS (UD-COSMOS) for NB816 (NB921) is shown in Figure 3. As expected, the completeness is lower at fainter magnitude in both BB and NB.

Aihara et al. (2017a) also measure the detection completeness by embedding synthetic objects with a PSF profile in coadded images directly and then running hscPipe to retrieve the embedded objects. Our measurement is consistent with theirs.

2.3.2 Dependence of NB response function on radius

Since the diameter of the HSC filters is as large as 60 cm, the filter response curve is slightly dependent on the position on the filter. The measurement of response curve at the various positions of the filter shows that the response curve can change along the radial direction and not along angular direction. The central wavelength and full width at half maximum (FWHM) of the response curve can become longer and wider by 14Å (15Å) and 4.0Å (4.5Å) at larger radius for NB816 (NB921), respectively. One should also refer to Kawanomoto et al. (2017), in prep. for the details of the HSC filters.

We compare the photometry between UD and D layer data for identical objects in an overlapping `patch` of the COSMOS field. Since the pointing coordinates are different between the UD and D layers, the objects in the region of the UD-COSMOS are observed in a position closer to the center of HSC FoV than those in the D-COSMOS. We make sure that no systematic difference is seen between the photometry. We also investigate the

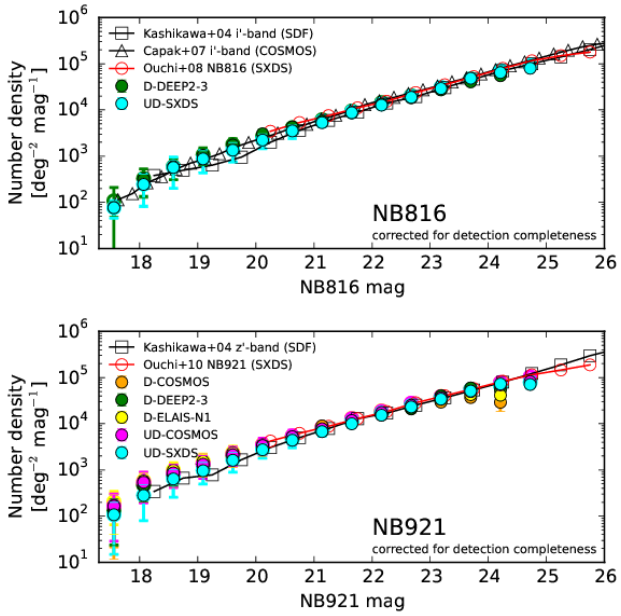

Fig. 4. Number counts of NB-detected galaxies. Open circles show the number densities of the galaxies detected in NB816 or NB921 regardless of detection in any other bands. Among the galaxies, the number densities of the NB-detected galaxies with detection in all of the BBs are shown by the filled circles. Note that the number densities are corrected for the detection completeness estimated in § 2.3.1. The objects with magnitudes brighter than 17.5 mag are rejected due to the saturation. The upper panel shows the NB816 data and the lower panel shows the NB921 data. The number counts are compared with the previous studies (Ouchi et al. 2008; Ouchi et al. 2010; Kashikawa et al. 2004; Capak et al. 2007).

dependence of the BB-NB colors in galaxies and stars and the number counts of NB-detected galaxies on the `patch`. All of the validation tests suggest that there is no significant impact of the slight non-uniformity in the filter response on the photometry of objects in the NBs, the detection of the objects in the NBs, and selection of NB emission-line galaxies.

2.3.3 Number counts

Number counts of detected galaxies are a useful tool to verify our detection and galaxy selection. Figure 4 shows the number densities of the NB-detected galaxies that we have selected in the NB816 and NB921 data. Both number densities in NB816 and NB921 show the similar behavior to each other. As expected, the number densities of galaxies increase up to about 24.5 (25.0) magnitudes in the D (UD) fields. The values are consistent with the limiting magnitudes shown in Table 1. In the range of 20–24 mag, the number densities of galaxies detected in individual D or UD fields are consistent with each other. This suggests that there is no significant field-to-field variance for the NB-detected galaxies within this magnitude range. However, there is larger variance at brighter magnitudes of < 20 mag. This is expected since the number of bright galaxies is small and thus the bright end of number densities is more sensitive to a field variance than the fainter part. The NB921 number densities in the UD fields show the slight difference, while those in the D fields show better consistency. Thus, it is important to survey area wider than ~ 2 deg^2 (1 FoV of the HSC) to overcome the field variance in bright galaxies.

As mentioned in § 2.2.1 (see also Appendix 1), we exclude bright objects when the central 3×3 pixels are saturated. Drake et al. (2013) point out the possibility that bright emission-line galaxies can be missed due to the magnitude cut at the bright end (see also Stroe et al. 2014). It is thus important to know the influence of the saturation limit on the bright end of the number counts. To estimate magnitudes where saturation occurs for extended sources, we compare the HSC-SSP catalogs with the COSMOS2015 catalog (Laigle et al. 2017) for objects with `flags_pixel_saturated_center=True` in NB921, and find that they have a 2" aperture magnitude in z' brighter than 17.3 mag in the COSMOS2015 catalog. The saturation magnitudes for point sources are discussed in Coupon et al. (2017). Therefore, we limit our samples to the objects with `cmodel` magnitude fainter than 17.5 mag conservatively.

We compare the number densities of the galaxies that we have selected with previous studies in general deep fields (Ouchi et al. 2008; Ouchi et al. 2010; Kashikawa et al. 2004; Capak et al. 2007). We compare our results with the number densities of galaxies detected in NB816 and NB921 of Subaru/Suprime-Cam in the SXDS field (Ouchi et al. 2008; Ouchi et al. 2010). They surveyed ~ 1 deg^2 with the similar NB filters to those of HSC down to 26 mag. We also compare with the number densities of galaxies detected in i (z) band for NB816 (NB921) detected galaxies, that is, galaxies detected in bands at similar wavelength are compared. Kashikawa et al. (2004) surveyed the SDF covering 0.25 deg^2, while Capak et al. (2007) observed the COSMOS field covering 2 deg^2. Since the number densities of emission-line galaxies showing an excess in BB-NB is much smaller than those of galaxies without the color excess, the comparison is meaningful in particular in the magnitude range of < 20 mag where the NB816 and NB921 number counts from the previous studies are not available. Figure 4 shows that the number densities of galaxies selected based on HSC-SSP data are consistent with the previous studies. This suggests that the object detection by hscPipe works well and the magnitude cut of 17.5 mag to avoid saturation is reasonable.

3 Emission-line galaxies at $z < 1.5$

The flux density observed in a spectral band where an emission line enters is expressed by the following: $f_{\lambda,\mathrm{band}} = f_{\lambda,\mathrm{cont}} + f_{\mathrm{el}}/\Delta_{\mathrm{band}}$, where f_λ is the flux density, $f_{\lambda,\mathrm{cont}}$ is for the stellar continuum, f_{el} is the emission-line flux, and Δ_{band} is the width of the filter. Magnitudes in NB are more sensitive to an

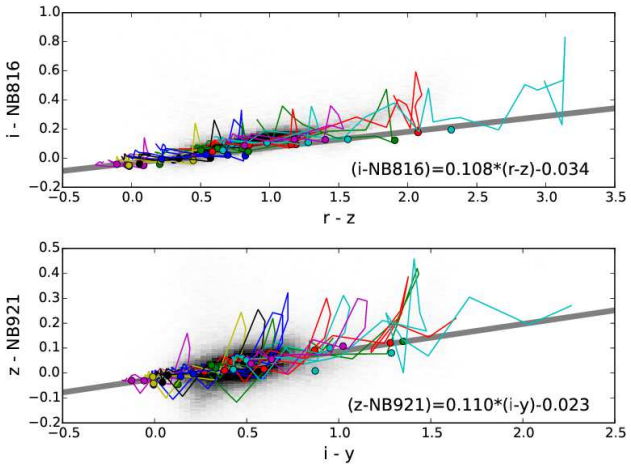

Fig. 5. Colors of stellar continuum in $i-$NB816 ($z-$NB921) for galaxies as a function of $r-z$ ($i-y$). Since the effective wavelength of NBs is different from that of BBs, galaxies with redder colors tend to show a larger value in the BB-NB colors which can mimic the color excess in emission-line galaxies. The thin lines show the color tracks of model spectra by Bruzual & Charlot (2003) for galaxies at $z=0$–2. The details of the model spectra are described in the text. The circles show the colors of galaxies at the specific redshifts that NB816 or NB921 can probe. The gray thick lines show a line fitted to the circles. In background, color distribution for galaxies with NB = 18–23 mag is shown in gray scale using HSC data, which is consistent with the model color tracks.

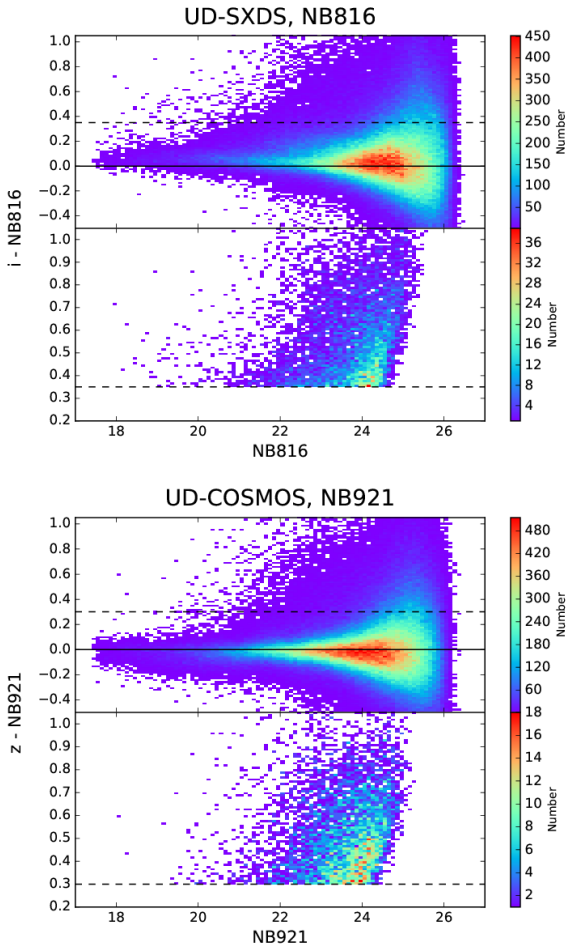

Fig. 6. Colors of $i-$NB816 ($z-$NB921) as a function of NB816 (NB921) magnitude in the UD-SXDS (UD-COSMOS) field. In each NB data, the upper panel shows the color distribution for galaxies, where the colors are corrected for the color term shown in Figure 5. The color coding is based on the number of galaxies in each bin. Although the sequence of galaxies without emission line is slightly shifted from $i-$NB816=0 for NB816 data, this shift is consistent with what is shown in Figure 5. The correction of the color term is optimized for emission-line galaxies at the redshifts that NB816 can probe. The correction by which galaxies are distributed around $i-$NB816=0 results in an overestimation of stellar continuum for the emission-line galaxies. The lower panel shows the color distribution for the emission-line galaxies selected. The dashed lines shows the color cut that we apply: i-NB816=0.35 and z-NB921=0.30.

emission line entering the filter than those in BB by a difference in the width of filter. Since the flux density of the stellar continuum also contributes to magnitudes in NB, emission lines selected by NB imaging are required to have not only flux but also EW large enough to make a difference between NB and BB magnitudes. In practice, galaxies with such an emission line at specific redshifts matched to a wavelength of the NB are observed significantly brighter in the NB than the closest BB (e.g., NB816 against i or NB921 against z). In this section, we select Hα emitters (HAEs) at $z\sim0.25$, [OIII] emitters (O3Es) at $z\sim0.63$, and [OII] emitters (O2Es) at $z\sim1.19$ from the NB816-detected galaxies, and HAEs at $z\sim0.40$, O3Es at $z\sim0.84$, and O2Es at $z\sim1.47$ from the NB921-detected galaxies (Table 2).

3.1 Selection

We compare the flux densities between i and NB816 for the NB816-detected galaxies (z and NB921 for the NB921-detected galaxies) to select the NB816 (NB921) emission-line galaxies. The flux densities measured in `unforced` photometry are used for the comparison. The flux densities in BB of i or z are dominated by the stellar continuum, while the flux densities in NB are dominated by the emission line if the line with an EW large enough to be detected enters the NB. We must keep in mind that the spatial distribution of regions emitting the nebular emission lines is not necessarily the same as that of the stellar component in a galaxy (Nelson et al. 2012; Nelson et al. 2016). The extended nebular emission galaxies such as [OII] blobs are one of the extreme cases (Brammer et al. 2013; Yuma et al. 2013; Yuma et al. 2017). As described in §2.1, one of the BBs is selected in a higher priority than NB as a reference band for the `forced` photometry by hscPipe in the case of $z<1.5$ galaxies with stellar continuum detected, although the situation may change for Lyα emitters that have no detection in some of bluer BBs. This means that the `forced` photometry is conducted based on the light profile of the stellar component. As a result, the comparison between the `unforced` fluxes in BB and NB allows us to properly estimate the contribution of the

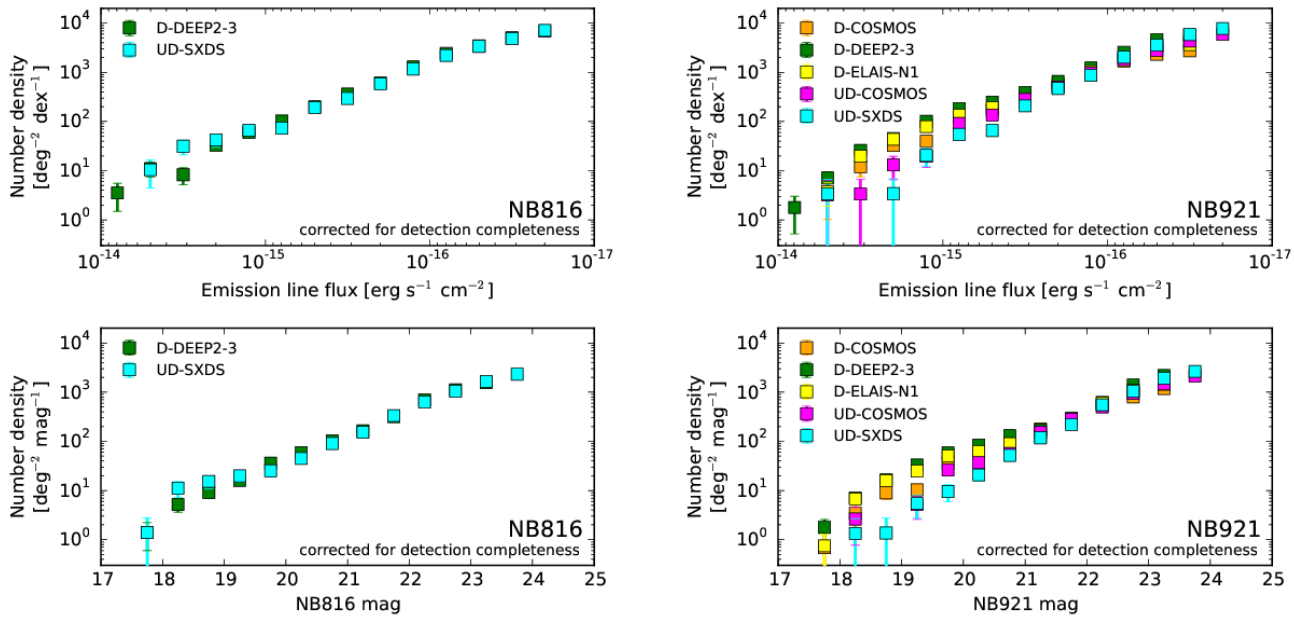

Fig. 7. Number counts of emission-line galaxies. The left two panels show the NB816 emitters and the right two panels show the NB921 emitters. The upper two panels are the number counts as a function of emission-line flux and the lower panels are the same but as a function of NB magnitude. The number densities are corrected for the detection completeness as estimated in § 2.3.1.

emission line to NB.

There is a slight difference in effective wavelength between i (z)-band and NB816 (NB921) (see Fig. 1), implying that the photometry in NB and BB results in the measurement of the flux densities at slightly different wavelengths. It is thus important to correct for the color term to properly estimate the stellar continuum underlying a emission line. Since the redder stellar continuum is more sensitive to the difference of the effective wavelength of the filter response function, the correction of color term should depend on the galaxy color. We use the stellar population synthesis models of Bruzual & Charlot (2003) to estimate the intrinsic colors of stellar continuum for galaxies at redshifts that the NB filters can probe. The color of $i-$NB816 ($z-$NB921) is investigated as a function of $r-z$ ($i-y$) color. Figure 5 shows the color tracks for the galaxies with simple stellar population (SSP) or constant star formation (CSF) with ages of 100Myr, 500Myr, 1Gyr and 3Gyr at $z=0$–2. We assume a dust extinction of $E(B-V)=0.0$ for the galaxies with SSP and $E(B-V)=0.0$ or 0.4 for the galaxies with CSF under the Calzetti et al. (2000) extinction curve. No emission line is taken into account in the model spectra, because we focus on the colors of stellar continuum. The color tracks indicate that there is a color variation at a given $r-z$ or $i-y$ color and some galaxies can have red BB-NB colors of more than 0.2. Since we focus on the emission-line galaxies at specific redshifts and prefer to avoid an overcorrection of the color term for the galaxies, we derive the relation between $i-NB816$ and $r-z$ ($z-NB921$ and $i-y$) by fitting the colors of the model galaxies at redshifts that the NB filters can probe (the gray line in Figure 5):

$$i-NB816 = 0.108(r-z) - 0.034 \quad (1)$$

for NB816-detected galaxies,

$$z-NB921 = 0.110(i-y) - 0.023 \quad (2)$$

for NB921-detected galaxies. The color distribution of the actual galaxies is consistent with the color tracks of the model galaxies. Therefore, we apply the color term to correct for the BB colors as a function of $r-z$ ($i-y$) for NB816 (NB921) detected galaxies as shown in Figure 5. The validity of this correction is supported by the result that the corrected BB-NB colors of galaxies are more tightly distributed around BB-NB=0 than before the correction (Figure 6).

We select galaxies with a difference between BB and NB magnitudes larger than 5σ uncertainty as shown in Figure 6. This 5σ cut is relevant at faint magnitudes. At bright magnitudes, Figure 5 suggests that bright galaxies with intrinsic red colors in the stellar continuum can be included as contaminants. We thus apply an additional cuts of i-NB816 > 0.35 and z-NB921 > 0.30. The color cuts are determined to exclude galaxies with spectroscopic redshifts located outside of the redshift ranges of possible NB emission-line galaxies. The criterion of the color cut is supported by the color tracks shown in Figure 5. The BB – NB of 0.35 (0.30) mag corresponds to an observed EW of 48Å (56Å) for NB816 (NB921) emitters. We further apply a requirement that objects are detected in all five broadbands (i.e., `merge_peak=True` and `detected_notjunk=True`).

This is because photometric redshifts or galaxy colors are required to distinguish between different emission lines, which is discussed in § 3.3. As a result, 8,597 and 18,310 candidates of NB816 emission-line galaxies are found in the UD-SXDS and D-DEEP2-3 fields, while 6,416, 6,074, 5,570, 15,909, and 11,856 candidates of NB921 emission-line galaxies are found in the UD-COSMOS, UD-SXDS, D-COSMOS, D-DEEP2-3, and D-ELAIS-N1 fields, respectively.

3.2 Number counts of emission-line galaxies

Figure 7 shows the number counts of emission-line galaxies. Based on these plots, we choose to apply magnitude cuts to ensure complete samples. We place a cut at 23.5 and 24.0 in the D and UD fields. The line fluxes are 2–3$\times10^{-17}$ erg s^{-1} cm^{-2} in the D fields, and 1.5–2$\times10^{-17}$ erg s^{-1} cm^{-2} in the UD fields. Note that these magnitudes are not the limiting magnitudes in the NB data itself but the magnitudes at the peak of the number counts of the emitters which ensures a high level of completeness. Indeed, the magnitudes are $\sim$1 mag shallower than the 5σ limiting magnitudes of NB816 and NB921. The imposition of detection in all BBs on the emitters also contributes to the difference with the limiting magnitudes of the NB detections themselves. For the NB816 emitters, the number counts are consistent with each other between the two fields. For the NB921 emitters, the number counts are consistent with each other between the fields at the faint end of $< 2 \times 10^{-16}$ erg s^{-1} cm^{-2} or > 21 mag. However, there is a large variation between the fields at the bright end (right panels of Figure 7), suggesting that the wide-area survey is essential to search for bright galaxies whose number density is small. Since we limit the samples to galaxies with NB magnitudes fainter than 17.5 mag, it is probable that we miss very bright NB816 (NB921) emitters (see also the discussion in Drake et al. 2013 and Stroe et al. 2014). The cut of 17.5 mag and BB-NB colors of 0.35 (0.30) that we apply in the selection of emission-line galaxies implies that most of NB816 (NB921) emitters with line fluxes larger than 5.5 (5.0) $\times$ 10^{-15} erg s^{-1} cm^{-1} cannot be selected.

3.3 Line identification

The NB816 and NB921 emission-line galaxies selected in § 3.1 could be identified with one of several strong nebular emission lines. Possible candidates are typical emission lines of Hα, [OIII], Hβ, and [OII] in rest-frame optical wavelengths from star-forming galaxies at the specific redshifts of $z = 0.2$–1.5 (Table 2).

We take three steps to identify emission lines. First, we use public spectroscopic redshifts available in the D and UD fields from the literature[2] which are incorporated into the HSC-SSP database (Takata et al. 2017, in prep.). We can identify a specific emission line as contributing to the excess flux in the NB data if a spectroscopic redshift is available and it agrees with the observed wavelength coverage of the NB filter. As shown in Table 2, the NB can probe a specific range of redshifts. If the spectroscopic redshift of the galaxy is within the range, the emission line is identified. Otherwise, if a redshift exists but is in disagreement with the NB line detection, the galaxy is excluded from the sample and considered a contaminant.

In addition, we use photometric redshifts and their errors to

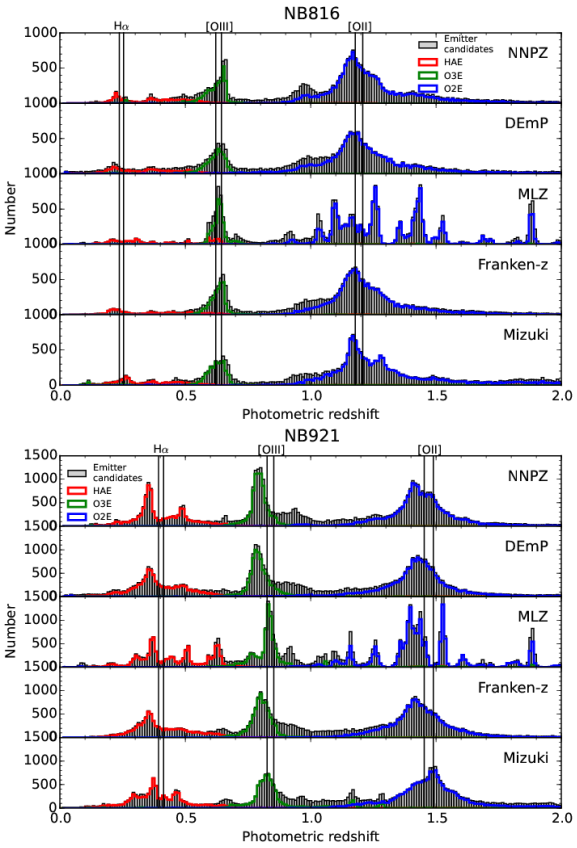

Fig. 8. Distribution of photometric redshift of galaxies selected as NB emission-line galaxy candidates in all of the D and UD fields (gray histograms), where five photometric redshifts calculated by different codes (MNPZ, DEmP, MLZ, Franken-z, and Mizuki; Tanaka et al. 2017) are available for individual galaxies. The upper panels are for the NB816 emitters and the lower panels are for the NB921 emitters. Among them, the galaxies with Hα, [OIII], [OII] emissions identified in § 3.3 are shown in red, green, and blue histograms, respectively.

[2] zCOSMOS DR3 (Lilly et al. 2009), UDSz (Bradshaw et al. 2013; McLure et al. 2013), 3D-HST (Skelton et al. 2014; Momcheva et al. 2016), FMOS-COSMOS (Silverman et al. 2015), VVDS (Le Fèvre et al. 2013), VIPERS PDR1 (Garilli et al. 2014), SDSS DR12 (Alam et al. 2015), WiggleZ DR1 (Drinkwater et al. 2010), DEEP2 DR4 (Davis et al. 2003; Newman et al. 2013), and PRIMUS DR1 (Coil et al. 2011; Cool et al. 2013).

identify emission lines. We calculate five independent sets of photometric redshifts by the different codes for the S15B internal release data (Tanaka et al. 2017). Among them, we use four sets for the line identification. One photometric redshift catalog (DEmP, Hsieh & Yee 2014) is not used because the uncertainties on the photometric redshifts are largely over-estimated[3]. However, note that there is no problem with the estimated photometric redshifts themselves. We thus use a combination of the four photometric redshifts in order to identify the emission line. First, we apply a photo-z quality cut appropriate for the individual photo-z sets, e.g., reduced $\chi^2 < 5$ for the `MIZUKI` code, to ensure that uncertain photo-z's are eliminated and only more likely photo-z's are used for the identification. If the galaxy meets the quality cut, we look for possible emission-line redshifts. If one of the emission-line redshifts is consistent within the photo-z 95% confidence interval, then we assign the galaxy to that emission line. If an object is consistent with multiple emission-line redshifts, we assign the object to the emission line at the redshift closest to the photo-z. Finally, we combine the four photo-z estimates; when three estimates or more agree on the emission-line redshift, we assign the redshift to that object. Otherwise, the galaxies are excluded from the sample. Figure 8 show the redshift distributions of emission-line galaxies for individual photometric redshifts. There are several peaks around the emission-line redshifts that we expect from the wavelength of NB (Table 2), which indicates that our method to select emission-line galaxies works well. However, we also note that the galaxies selected as a NB816 emitter show the peak at $z \sim 1.0$, which is not expected. The peak is likely due to red galaxies with strong Balmer/4000Å break being incorrectly selected as an emission-line galaxy (Figure 5). The contamination of the strong Balmer/4000Å break galaxies is also reported by Sobral et al. (2012). Because the effective wavelength of NB is longer than that of BB, if galaxies without emission line have the strong continuum break between the effective wavelengths of BB and NB, the NB magnitude can be brighter than the BB magnitude significantly. Although we correct the BB magnitudes for the color term to not select such galaxies with red continuum colors as discussed in §3.1, the color term correction is optimized for galaxies at the specific redshifts that the NBs can probe. Figure 5 suggests that the correction can be underestimated for galaxies at other redshifts. Furthermore, since the i-band filter is wider than the z-band and the difference of effective wavelength between BB and NB is larger for the pair of i and NB816, the $i-$NB816 colors are easier to select such red galaxies than the $z-$NB921 colors. It is difficult to distinguish the NB816 O2Es at $z \sim 1.2$ from the red galaxies at $z \sim 1$ based on the two color diagrams shown below. There is another small peak at the redshift next to the [OIII] line, i.e., $z \sim 0.7$ for NB816 and $z \sim 0.9$ for NB921. This is likely that for Hβ emission-line galaxies. Therefore, Figure 8 indicates that the line identification based on the photometric redshift is effective in reducing contamination, as discussed in more detail in § 3.4.

[3] This issue is only for the S15B internal data release and the DEmP photo-z's in PDR1 do not have such an issue.

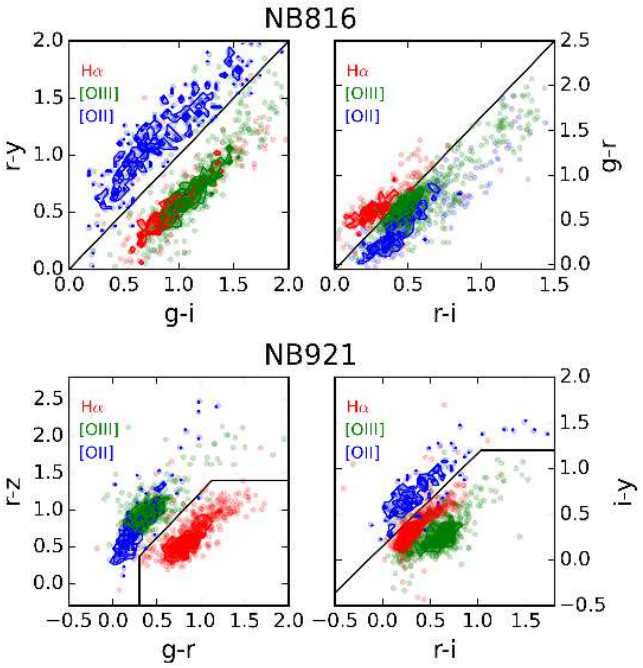

Fig. 9. Color–color diagrams used for line identification. The upper panels are the diagrams for NB816 emitters, and the lower panels are for NB921 emitters. In each panel, emission-line galaxies with spectroscopic redshifts in all of the fields are plotted. Individual galaxies are shown as fainter symbols and the contours are shown in solid lines for Hα in red, [OIII] in green, and [OII] in blue. For NB816 emitters, O2Es at $z \approx 1.19$ are distinguished from the others based on $g-i$ vs. $r-y$, and then HAEs at $z \approx 0.25$ are distinguished from O3Es at $z \approx 0.63$ based on $r-i$ vs. $g-r$. For NB921 emitters, HAEs at $z \approx 0.40$ are distinguished from the others based on $g-r$ vs. $r-z$, and then O2Es at $z \approx 1.47$ are distinguished from O3Es at $z \approx 0.84$ based on $r-i$ vs. $i-y$. The boundaries are specified in the text.

Finally, if the galaxy is not identified yet based on the information on spectroscopic and photometric redshifts, we use colors to identify emission line as shown in Figure 9. This case can apply to galaxies with faint stellar continuum or galaxies with strong emission lines that impact on the BB magnitudes. The colors of the galaxies are measured with magnitudes in `forced` photometry, because we are now interested in the colors of stellar continuum. For NB816 emitters, we use $g-i$ versus $r-y$ colors to distinguish [OII] at $z \sim 1.19$ from the others:

$$(r-y) > (g-i), \tag{3}$$

and then $r-i$ versus $g-r$ colors to distinguish Hα at $z \sim 0.25$ from [OIII] at $z \sim 0.63$:

$$(g-r) > 1.7(r-i) - 0.05. \tag{4}$$

For NB921 emitters, we use $g-r$ versus $r-z$ colors to distin-

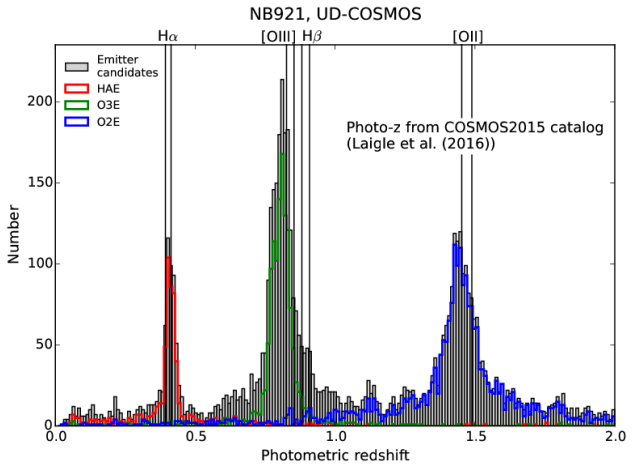

Fig. 10. Same as Figure 8, but for NB921 emitters in the UD-COSMOS field. The photometric redshifts are from the COSMOS2015 catalog (Laigle et al. 2016) instead of those estimated from HSC-SSP data.

guish Hα at $z \sim 0.40$ from the others:

$$(g-r) > 0.3 \ \wedge \ (r-z) < 1.4 \ \wedge \ (r-z) < 1.24(g-r), \quad (5)$$

and then $r-i$ versus $i-y$ colors to distinguish [OII] at $z \sim 1.47$ from [OIII] at $z \sim 0.84$:

$$(i-y) < 1.2 \ \wedge \ (i-y) < 1.02(r-i) + 0.15. \quad (6)$$

The color criteria are determined based on the colors for emission-line galaxies with spectroscopic redshifts.

3.4 Validation of the line identification

To validate our selection and line identification, we use the galaxies that are selected as NB emission-line galaxies in § 3.1 and have spectroscopic redshifts. We find that among 84 NB816-HAEs with a spectroscopic redshift at $z \approx 0.25$, 343 NB921-HAE at $z \approx 0.40$, 203 NB816-O3Es at $z \approx 0.63$, 274 NB921-O3E at $z \approx 0.84$, 199 NB816-O2Es at $z \approx 1.19$ and 109 NB921-O2E at $z \approx 1.47$, our identification with photometric redshifts and BB colors selects 94% of the NB816-HAEs at $z \approx 0.25$, 85% of the NB921-HAEs at $z \approx 0.40$, 77% of the NB816-O3Es at $z \approx 0.63$, 84% of the NB921-O3Es at $z \approx 0.84$, 93% of the NB816-O2Es at $z \approx 1.19$ and 88% of the NB921-O2Es at $z \approx 1.47$. The results indicate that the high fraction of emission-line galaxies without spectroscopic redshift can be properly identified. On the other hand, the identification with photo-z's or colors can contain 33% of the contaminants with an inappropriate spectroscopic redshift in the NB816-HAEs sample, 17% in the NB921-HAE sample, 13% in the NB816-O3E sample, 15% in the NB921-O3E sample, 40% in the NB816-O2E sample and 43% in the NB921-O2E sample. The O2E samples can contain the relatively large fraction of contamination compared with the samples of the other lines. This is because since the [OII] doublet at $\lambda\lambda = 3727, 3730$Å are located near the Balmer/4000Å break, it is hard to estimate the stellar continuum level underlying the line only with the photometric data and the BB-NB colors of strong Balmer/4000Å break galaxies are easy to mimic those of emission-line galaxies as discussed in the previous section.

Figure 10 shows the photometric redshift distribution of emission-line galaxies in the UD-COSMOS. As a further test, we use the many-band photometric redshifts from the COSMOS2015 catalog (Laigle et al. 2017), which are available for essentially all the NB emitters. Because the photometric redshifts in the COSMOS2015 catalog are estimated from 30-band photometry covering wide wavelengths from NUV to MIR, they are more precise ($\sigma(\Delta z/(1+z)) \sim 0.007$: Laigle et al. 2017) than the photometric redshifts from 5-band photometry of the HSC-SSP ($\sigma(\Delta z/(1+z)) \sim 0.05$: Tanaka et al. 2017). Therefore, the distribution with the sharp peaks at the expected redshifts also indicate the validity of our selection and line identification of emission-line galaxies (see also Figure 8).

In our line identification, we distinguish [OIII] from Hβ based on the photometric redshifts, because it is impossible to do that based on the color–color diagrams (Figure 9). We estimate an amount of Hβ emitters that can be included in the O3E sample. Among 14 Hβ emitters at $z \sim 0.68$ and 39 Hβ emitters at $z \sim 0.89$, which are classified by the spectroscopic redshifts, 43% of Hβ emitters at $z \sim 0.68$ and 21% of Hβ emitters at $z \sim 0.89$ are identified as O3Es based on the photometric redshifts and colors. However, among the contamination in the O3E samples, the fraction of Hβ emitters are less than 25%. Therefore, we conclude that the contamination of Hβ emitters in the O3Es sample is not so severe. Figure 8 also support our line identification between [OIII] and Hβ.

3.5 AGN contamination

Since an AGN can contribute to the strong nebular emission lines from galaxies, objects with an emission line detected by the NB imaging can be AGNs, not star-forming galaxies. Sobral et al. (2016) find by spectroscopy that 30% of luminous HAEs at $z = 0.8$–2.2 can be AGN and the fraction of AGN increases with Hα luminosity at $L(\mathrm{H}\alpha) > 10^{42}$ erg s^{-1}. The trend is not dependent on the redshifts of HAEs. Other previous studies have reported several percent of X-ray detected AGN contamination in the NB emitter samples (e.g., Garn et al. 2010; Calhau et al. 2017; Matthee et al. 2017). It is thus important to estimate the fraction of AGNs in the samples of emission-line galaxies that we have selected.

We use the 4.6 Ms X-ray data by the Chandra COSMOS-Legacy Survey (Civano et al. 2016) which almost fully covers the UD-COSMOS field. The D-COSMOS field is partially covered. Marchesi et al. (2016) present the catalog of 4016 X-

Table 3. Samples of emission-line galaxies. The number of emission-line galaxies with a NB magnitude and an emission-line flux brighter/larger than the limit above which the sample is complete (§ 3.2) is shown. Magnitudes are given in units of AB mag, fluxes are in units of erg s^{-1} cm^{-2}, and the survey volumes are in units of comoving Mpc^3 h_{70}^{-3}. The value within the parenthesis shows the number and volume for the area excluding the overlapping regions between UD-COSMOS and D-COSMOS fields.

Hα emitters (HAEs)

	NB816 ($z = 0.25$)				NB921 ($z = 0.40$)			
Field	# of objects	mag cut	flux cut	Volume	# of objects	mag cut	flux cut	Volume
UD-COSMOS	···	···	···	···	471	24.0	2.0×10^{-17}	1.5×10^5
					(441)			(1.5×10^5)
UD-SXDS	304	24.0	1.5×10^{-17}	5.0×10^4	422	24.0	2.0×10^{-17}	1.2×10^5
D-COSMOS	···	···	···	···	974	23.5	3.0×10^{-17}	5.3×10^5
					(772)			(4.2×10^5)
D-DEEP2-3	889	23.5	2.0×10^{-17}	4.5×10^5	2,915	23.5	3.0×10^{-17}	2.0×10^6
D-ELAIS-N1	···	···	···	···	2,311	23.5	3.0×10^{-17}	1.6×10^6

[OIII] emitters (O3Es)

	NB816 ($z = 0.63$)				NB921 ($z = 0.84$)			
Field	# of objects	mag cut	flux cut	Volume	# of objects	mag cut	flux cut	Volume
UD-COSMOS	···	···	···	···	1,127	24.0	2.0×10^{-17}	5.5×10^5
					(1,074)			(5.2×10^5)
UD-SXDS	894	24.0	1.5×10^{-17}	2.9×10^5	762	24.0	2.0×10^{-17}	4.6×10^5
D-COSMOS	···	···	···	···	851	23.5	3.0×10^{-17}	1.6×10^6
					(609)			(1.3×10^6)
D-DEEP2-3	1,334	23.5	2.0×10^{-17}	2.5×10^6	2,409	23.5	3.0×10^{-17}	6.4×10^6
D-ELAIS-N1	···	···	···	···	1,574	23.5	3.0×10^{-17}	5.3×10^6

[OII] emitters (O2Es)

	NB816 ($z = 1.19$)				NB921 ($z = 1.47$)			
Field	# of objects	mag cut	flux cut	Volume	# of objects	mag cut	flux cut	Volume
UD-COSMOS	···	···	···	···	1,309	24.0	2.0×10^{-17}	1.0×10^6
					(1,246)			(9.9×10^5)
UD-SXDS	1,868	24.0	1.5×10^{-17}	6.9×10^5	2,230	24.0	2.0×10^{-17}	9.0×10^5
D-COSMOS	···	···	···	···	1,447	23.5	3.0×10^{-17}	3.3×10^6
					(1,222)			(2.6×10^6)
D-DEEP2-3	3,993	23.5	2.0×10^{-17}	5.9×10^6	3,055	23.5	3.0×10^{-17}	1.2×10^7
D-ELAIS-N1	···	···	···	···	3,263	23.5	3.0×10^{-17}	1.1×10^7

ray sources, 97% of which have an optical/IR counterpart. We match our catalogs to the X-ray sources and then find that few emission-line galaxies ($\sim$ 0.1%) have a counterpart of X-ray source. The luminosities of emission line of galaxies with an X-ray counterpart is not so large, which is against our expectation that AGNs can have a large contribution to the bright end of luminosity functions (discussed more in § 5.2). Also, the fraction of emission-line galaxies with an X-ray counterpart does not depend on the line, i.e., Hα, [OIII], or [OII].

As mentioned in § 2.2.3 and § 2.3.3, we remove the objects with NB `cmodel` magnitudes brighter than 17.5 or point sources from the catalogs. Removing the objects may result in removing AGNs unintentionally from the samples of NB emitters and that may explain the small fraction of the emission-line galaxies with X-ray counterpart. To investigate this possibility, we match the removed objects to the X-ray source catalog in the UD-COSMOS field. We find that among 4016 X-ray sources, 369 NB921-detected point sources (9.2%) and 93 objects saturated in NB921 data (2.3%) are counterparts of the X-ray sources. Although five point sources meet the criteria of the EW cut (i.e., z-NB921$>$0.3), only one source has the spectroscopic or photometric redshifts consistent with those of NB921 emitters. Therefore, we conclude that there is no impact of the removal of the point sources and the saturated objects on the discussion of AGNs in the NB emitter samples.

The COSMOS data indicates the fraction of X-ray detected AGN contamination is small, which is $\sim 0.1\%$. We assume that the contamination rate in the other fields is the same as in the COSMOS field. Even if there are 0.1% of AGNs in the samples, our results such as luminosity function do not change largely.

3.6 Stellar mass of emission-line galaxies

We calculate stellar mass for the emission-line galaxies by SED fitting with five HSC BB data using the code with Bayesian priors called 'MIZUKI' (Tanaka 2015). If galaxies have a spectroscopic redshift, the SED fitting is performed at the fixed redshift. Otherwise, we fix a redshift to that estimated from the wavelength of NB (e.g., $z = 0.40$ for NB921 HAEs, see also Table 2). The model SED templates of galaxies are generated by the code of Bruzual & Charlot (2003) and emission lines are taken into account. Metallicity is fixed to the solar value and the extinction curve of Calzetti et al. (2000) is adopted. Ages and optical depth in the V-band ranges 0.05–14 Gyr and 0–2, respectively. Star formation histories of exponentially declining model with a decay timescale of 0.1 – 11 Gyr, SSP model, and constant SFR model are adopted. Note that the reddest HSC BB (i.e., y-band whose effective wavelength is 9755Å) corresponds to the data at $\sim$ 4000–4500 Å in the rest frame for O2Es at $z = 1.19$–1.47. We significantly suffer from the degeneracy between age, metallicity, and dust extinction. Thus, we impose no dust extinction only for the O2Es at $z = 1.19$–1.47. The assumption is not unreasonable, because O2Es at $z \sim 1.5$ are likely to be less dusty star-forming galaxies (Hayashi et al. 2013).

We compare the stellar masses estimated from the five HSC BBs with those from the more multi-wavelength data in the COSMOS2015 catalog (Laigle et al. 2016). Note that the same IMF (Chabrier 2003) is assumed. We find that our stellar masses are in good agreement with those of the COSMOS2015 catalog for the HAEs, while our stellar masses are systematically larger by a factor of ~ 2 at the most for the O3Es and O2Es. This is a known bias of the code (Tanaka 2015) and it will likely be reduced in our future runs. However, this may also imply that multi-band data at longer wavelength such near-infrared (NIR) data are required to estimate more accurate stellar masses for the O3Es and O2Es at $z \gtrsim 0.8$. To keep the consistency in data set and photometry with hscPipe between the fields, we use only the HSC data in this paper. The studies with u-band and NIR data are planned in the next data release (Aihara et al. 2017a). On the other hand, the systematic difference by a factor of ~ 2 can be caused by the different codes used for the SED fitting even if the same data set is used (Behroozi et al. 2010). The stellar masses that we estimate with the five BBs for the emission-line galaxies are reliable for the HAEs and those for the O3Es and O2Es can still be used with a caveat that there is a possible systematic difference by a factor of ~ 2.

3.7 Summary of catalogs of emission-line galaxies

We have identified 8,054 Hα emitters at $z \approx 0.25$ and 0.40, 8,656 [OIII] emitters at $z \approx 0.63$ and 0.84, and 16,877 [OII] emitters at $z \approx 1.19$ and 1.47 from NB816 and NB921 data down to the limit of magnitude and line flux where the samples are complete. The line fluxes above the completeness limit correspond to the observed luminosities larger than $\log(L/(\mathrm{erg\ s^{-1}})) \gtrsim 39.4$ and 40.1 in Hα at $z \approx 0.25$ and 0.40, $\log(L/(\mathrm{erg\ s^{-1}})) \gtrsim 40.4$ and 40.8 in [OIII] at $z \approx 0.63$ and 0.84, and $\log(L/(\mathrm{erg\ s^{-1}})) \gtrsim 41.1$ and 41.4 in [OII] at $z \approx 1.19$ and 1.47. These are among the largest samples ever constructed. The samples that we have selected are summarized in Table 3. Among the emission-line galaxies, $\sim$3.9% are identified by the spectroscopic redshift, $\sim$71.5% are by the photometric redshift, and $\sim$24.6% are by colors. The catalogs are available at the HSC-SSP data release site[4], after the paper is published.

4 Results

4.1 Spatial distribution of emission-line galaxies

Figures 11–13 show the spatial distribution of HAEs, O3Es, and O2Es at each redshift in each field, where the emission-line galaxies with NB magnitude brighter than and emission-line flux larger than the limits shown in Table 3 are plotted to ensure homogeneity of the depth and completeness over the fields surveyed. The figures clearly show that the individual populations of emission-line galaxies are not distributed uniformly but constitute large-scale structures over the fields surveyed. The scale of some structures are larger than the ~ 1.5 degree diameter of the HSC FoV, which corresponds to $\sim$50 comoving Mpc at $z \sim 0.4$ (e.g., HAEs in the D-DEEP2-3 field shown in Figure 11). Evidently, HSC can allow us to reveal large-scale structures which are hard to be fully identified even with Subaru/Suprime-Cam with a smaller FoV (0.57×0.45 deg^2). In each field, there are several overdense regions which seem to be located at the intersection of the filamentary structures of emission-line galaxies. This is a similar picture to what the hierarchical structure formation predicts (e.g., Vogelsberger et al. 2014; Schaye et al. 2015; Ishiyama et al. 2015).

It is interesting to compare the cosmic web of star-forming galaxies with the location of massive galaxy clusters. Oguri et al. (2017) search for galaxy clusters with the number of member galaxies larger than 15 up to $z \sim 1.1$ in the HSC Wide and Deep fields by using a red-sequence galaxy finder algorithm named CAMIRA (Cluster finding Algorithm based on Multi-band Identification of Red-sequence gAlaxies: Oguri 2014). We match our emitters to the catalog of the CAMIRA clusters. The clusters, identified with photometric redshift estimates matched to the NB selected galaxies, are plotted in Figures 11–13 with yellow star symbols.

Few CAMIRA clusters are found in the overdense regions of the HAEs at $z \approx 0.25$ and 0.40. It is known that the central region of galaxy clusters at $z < 1.0$ tends to be dominated by red quiescent galaxies and the regions where active star formation occurs move to the galaxy group environment in the outskirt of

[4] https://hsc-release.mtk.nao.ac.jp/

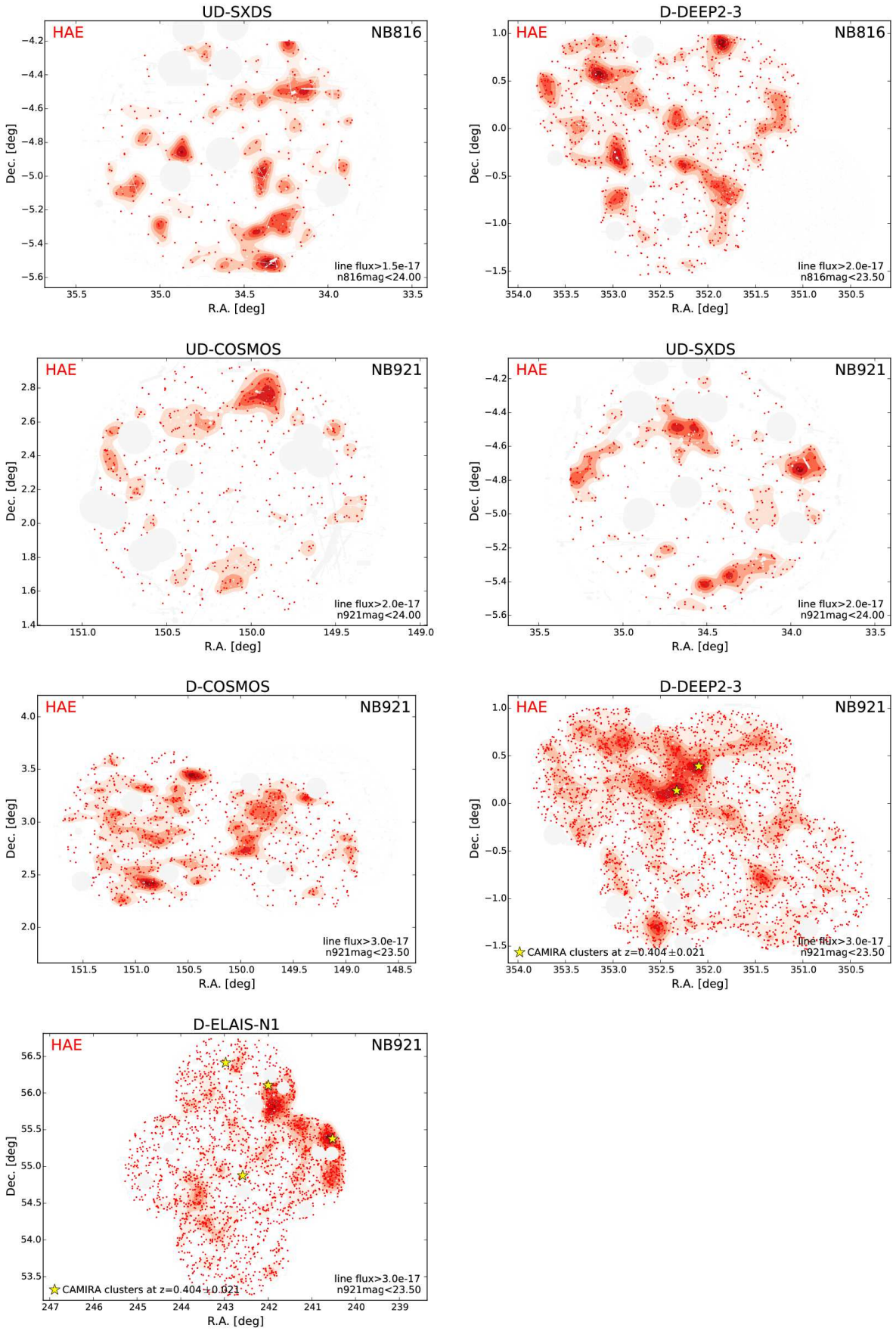

Fig. 11. Spatial distribution of the HAEs at $z \approx 0.25$ (for NB816) and 0.40 (for NB921) in each fields. The dots show the individual emission-line galaxies, whose number densities are shown by the contours. The gray regions are masked as described in §2.2.2. Star symbols show galaxy clusters at redshifts corresponding to $\lambda_c \pm \Delta\lambda$ of the NB, which are discovered from the red-sequence galaxies by the CAMIRA code (Oguri 2014; Oguri et al. 2017).

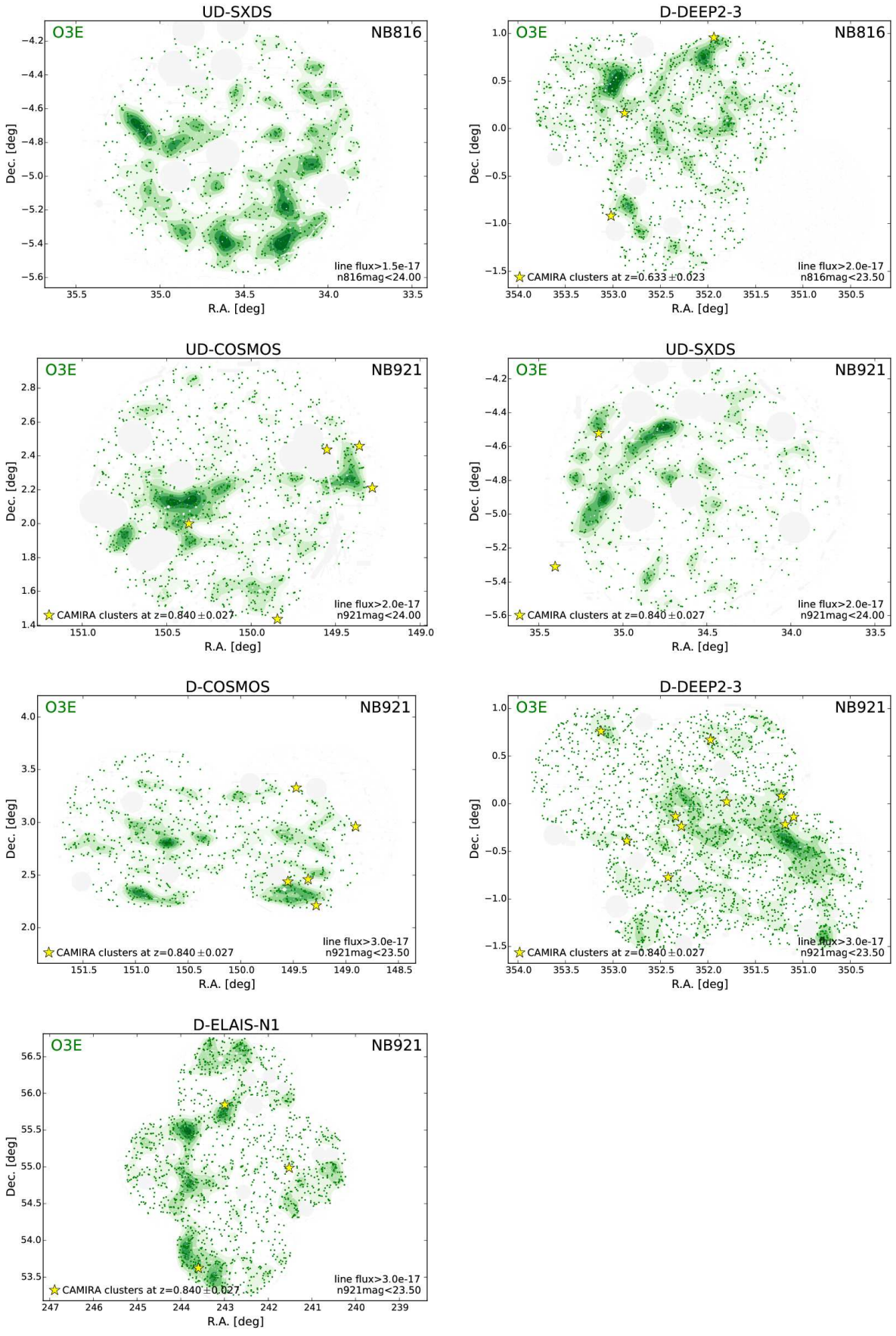

Fig. 12. The same as Figure 11, but for the O3Es at $z \approx 0.63$ (for NB816) and 0.84 (for NB921).

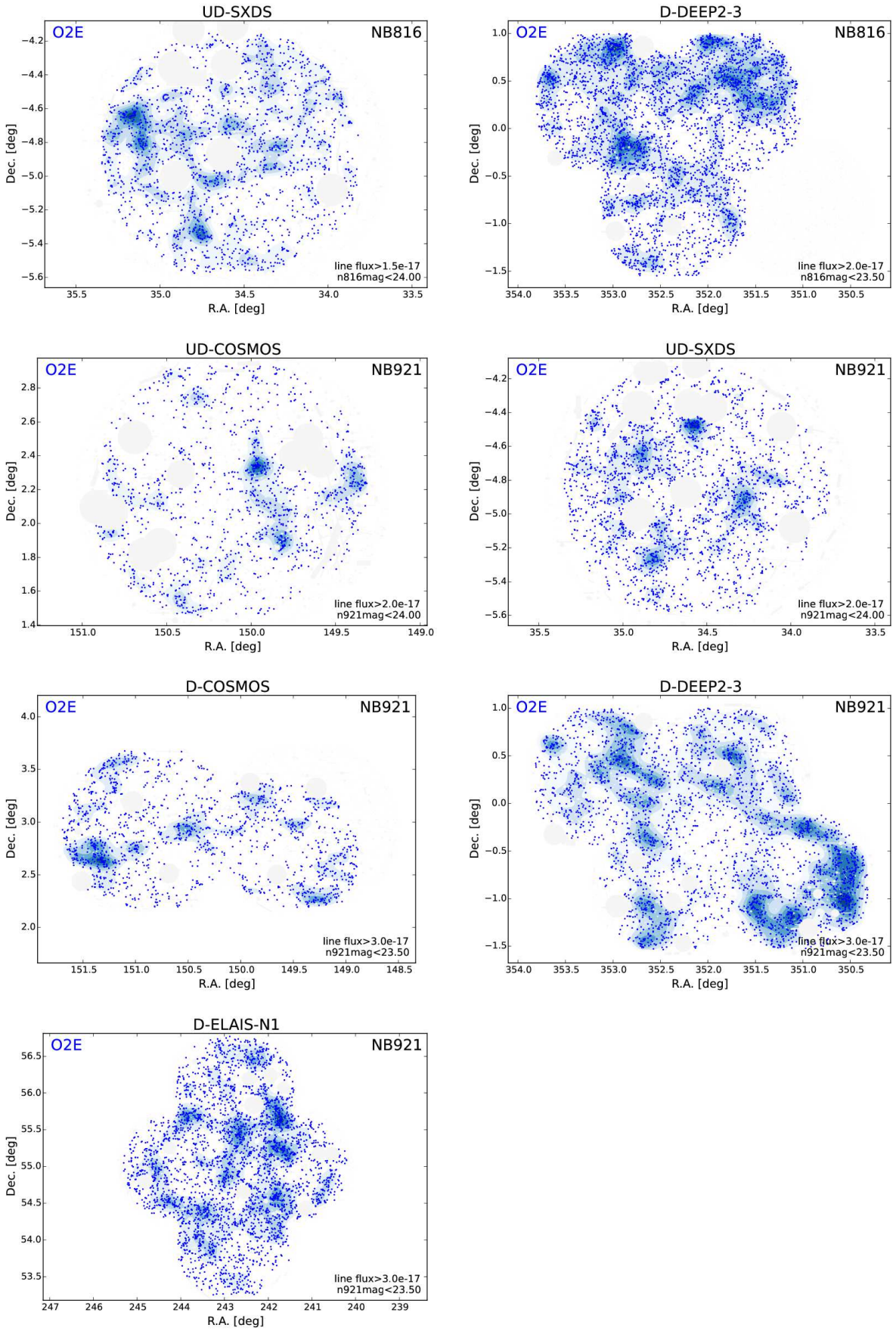

Fig. 13. The same as Figure 11, but for the O2Es at $z \approx 1.19$ (for NB816) and 1.47 (for NB921). Note that the comparison with the CAMIRA clusters is not performed for these plots. This is because the CAMIRA code identifies the galaxy clusters at only $z < 1.1$ with the currently available data.

the clusters and/or general fields (Koyama et al. 2010; Koyama et al. 2011). Star forming galaxies may not be the best tracer of clusters at these redshifts, but in the D-ELAIS-N1 field, there are four CAMIRA clusters at the edge of redshifts that the NB921 can probe (Figure 11). The regions surrounding the clusters are overdense in HAEs, that may indicate that the HAEs are located so that they connect the clusters. Of equal interest, we have found a super cluster that consists of two CAMIRA clusters at $z \approx 0.41$ embedded in the large-scale structures of HAEs in the D-DEEP2-3 field (see Figure 11). The separation between the clusters of similar redshift suggests that they are likely merging clusters and thus may have active star formation even in the central region of the clusters. The filamentary structures are spread out from the clusters. This structure including two galaxy clusters should be one of the interesting regions to investigate the environmental dependence of galaxy properties, which is discussed in another paper by Koyama et al. (2017). HAEs in the merging clusters at $z \sim 0.15$–0.3 are also investigated by Stroe et al. (2017) (see also Stroe et al. 2015).

Figure 12 shows that the O3Es at $z \approx 0.63$ and 0.84 do not solely trace galaxy clusters. However, the CAMIRA clusters at $z \sim 0.63$ and 0.84 are found along the large-scale distribution of the O3Es. [OIII] emission may not be the best indicator of SFR, because there can be a contribution from an AGN and [OIII] emitting galaxies can be biased towards less massive galaxies. However, the O3Es seem to trace the cosmic web connecting the galaxy clusters.

We have not searched for galaxy cluster at $z \gtrsim 1.1$ with the CAMIRA code due to lack of NIR data. At $z > 1$, it is known that active star formation occurs in the central region of galaxy clusters (e.g., Hayashi et al. 2010; Hilton et al. 2010; Brodwin et al. 2013), and we may expect that overdense regions of NB emitters can indicate the sites of clusters. Indeed, there are several overdensity regions of O2Es in each field, all of which are strong candidates of galaxy clusters at $z \approx$1.2–1.5. Follow-up spectroscopy is required to identify galaxy clusters where the O2Es are concentrated.

4.2 Luminosity function

4.2.1 Luminosities of emission lines

Fluxes of the emission lines are derived from the NB and BB photometry:

$$F_{\rm line} = \frac{\Delta_{NB} \cdot \Delta_{BB}}{(\Delta_{BB} - \Delta_{NB})} (f_{\lambda,NB} - f_{\lambda,BB}), \quad (7)$$

where $F_{\rm line}$ is a line flux, Δ is a FWHM of the filter in units of Å (see Table 2 for NBs, and Δ_{BB} = 1555 and 782 for i and z bands), and f_λ is a flux density in units of erg s^{-1} cm^{-2} Å^{-1}. As discussed in §3.1, the `cmodel` magnitudes in `unforced` photometry are used for the flux estimation. To measure the line fluxes according to the equation (7), it is assumed that the same stellar continuum level underlying emission lines contributes to the flux densities of $f_{\lambda,BB}$ and $f_{\lambda,NB}$. This implies that the difference of effective wavelength between BB and NB can affect the measurement of fluxes, in particular, for [OII]λ3727 doublet being near the Balmer/4000Å break or emission lines of red galaxies. Thus, as in § 3.1, we use the BB magnitudes corrected for the color term to calculate the fluxes of the emission lines. We use the best-fitting model spectra from the SED fits with all the BB filters, and we find that the stellar continuum underlying an emission line estimated from BB magnitudes are consistent with the model spectra. In what follows, we use the continuum estimated from the adjacent BB filters. The fluxes measured are converted to the luminosities using the spectroscopic redshifts, if available. Otherwise, we use the redshifts estimated from the NB to derive the luminosities.

There are [NII]($\lambda\lambda$=6550,6585Å) doublet lines next to the Hα line. While the width of NB is narrow, the targeted line and the adjacent lines can be simultaneously observed with the NB. In general, the fluxes of the contaminant emission lines are small compared with the targeted line of Hα. However, it is important to estimate how much the contamination contributes to the measurement of the fluxes of the targeted line. The contribution of [NII] line is estimated from the SDSS Data Release 7 (DR7) spectroscopic catalogs (Kauffmann et al. 2003; Salim et al. 2007; Abazajian et al. 2009). We select analogs of the HAEs by applying the same rest-frame EW cut to the SDSS spectroscopic data and investigate the [NII]/Hα line ratio as a function of stellar mass and observed Hα luminosity for the analogs (see the details in Appendix 2). We correct the line fluxes for the contribution of [NII] lines in the HAEs based on the stellar mass and the observed Hα luminosity of the individual galaxies. The median values of the fraction of [NII] over Hα+[NII] ranges 0.08–0.14 for NB816 and NB921 HAEs in each field. Although we note that Villar et al. (2008) and Sobral et al. (2012) have presented the correction of [NII] contribution based on the EW of Hα+[NII], we apply the method, described above, to estimate the line ratios such as [NII]/Hα and Hβ/Hα consistently throughout the paper (see also § 4.2.4 and Appendix 2).

4.2.2 Survey volume

Since the transmission curve of HSC NB filters is not a perfect top-hat (Figure 1), emission lines at different redshifts go through a different transmittance. Given that only emission lines with fluxes above a limiting flux can be detected, emission lines with an intrinsically large flux can be at lower or higher redshifts than fainter emission lines. Therefore, the survey volume for an emission-line galaxy depends on its luminosity.

We estimate the survey volume for individual emission-line galaxies. For a given luminosity, the minimum and maximum redshifts where the emission line can be observed at more than

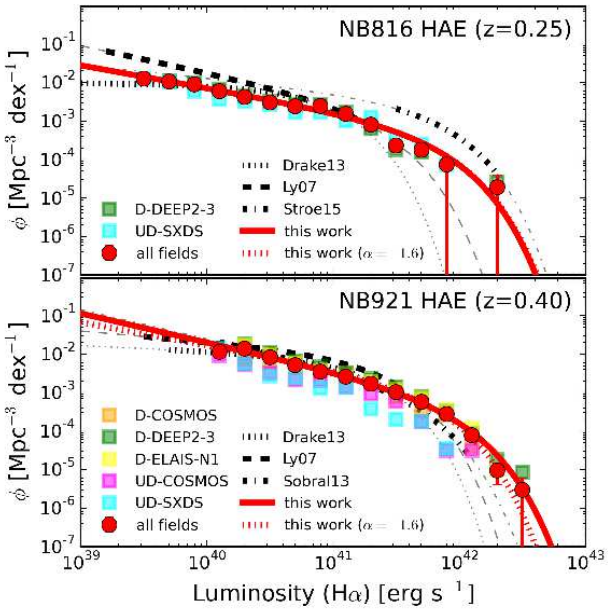

Fig. 14. Observed luminosity function of HAEs. The upper panel shows the luminosity function for NB816 HAEs at $z \approx 0.25$, while the lower panel shows that for NB921 HAEs at $z \approx 0.40$. The squares show the data in the individual fields with different colors. The red circles show the data in all of the fields surveyed and the error bars are estimated from the Poisson errors. The red curve is a best-fit Schechter function to the red data points, where the solid (dotted) curve is fitted without (with) α fixed. The black curves are the luminosity functions from the literature, where the luminosity range covering the data in each study is shown by thick curve and the other range is shown by thin curve (Ly et al. 2007; Drake et al. 2013; Stroe & Sobral 2015; Sobral et al. 2013).

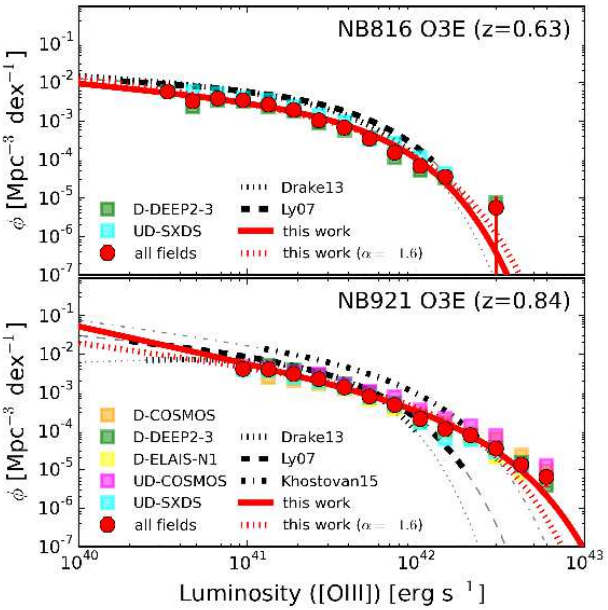

Fig. 15. The same as Figure 14, but for O3Es at $z \approx 0.63$ and 0.84. The luminosity functions from the literature (Ly et al. 2007; Drake et al. 2013; Khostovan et al. 2015) are plotted for comparison.

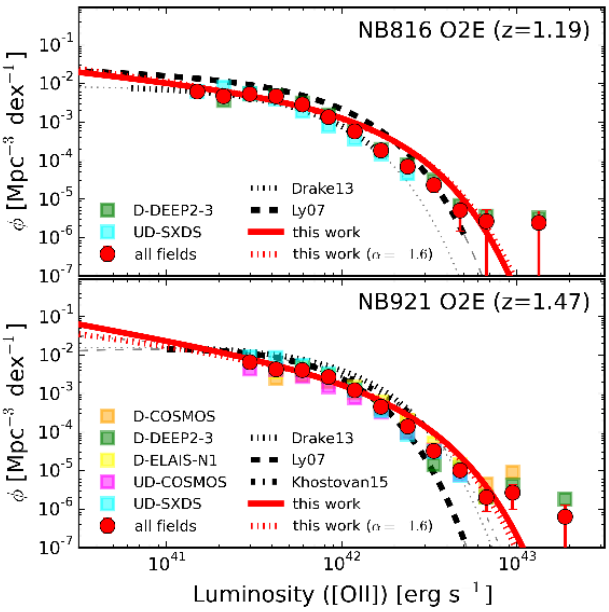

Fig. 16. The same as Figure 14, but for O2Es at $z \approx 1.19$ and 1.47. The luminosity functions from the literature (Ly et al. 2007; Drake et al. 2013; Khostovan et al. 2015) are also plotted for comparison.

5σ are calculated based on the filter transmission curve and a limiting flux. Then, the redshift range is converted to a comoving volume. Galaxies with brighter lines have a larger survey volume. The median survey volume in each field is shown in Table 3.

Note that we assume that the emission line is observed at the central wavelength of the NB filter. Given the fact that the NB filters do not have a perfect top-hat shape of transmission curve, intrinsic luminosity can be larger than observed luminosity. This results in underestimating (overestimating) the number of emission-line galaxies with bright (faint) intrinsic luminosities. Also, the survey volume can be underestimated for galaxies with an intrinsically larger luminosity. However, spectroscopic redshift is required to exactly know at which wavelength within the NB filter the emission line is observed. While some galaxies have the spectroscopic redshifts, most of the emission line galaxies do not have. Therefore, we apply the same survey volume to emission-line galaxies with a given observed luminosity.

4.2.3 Observed luminosity function

The luminosity function of emission-line galaxies is derived according to the V_{max} method:

$$\phi(\log L) = \sum_i \frac{1}{V_{max} \cdot f_c \cdot \Delta(\log L)}, \quad (8)$$

Table 4. Parameters of the Schechter function fitted to the luminosity function.

		No correction for dust extinction			Corrected for dust extinction		
	redshift	$\log\phi^*$	$\log L^*$	α	$\log\phi^*$	$\log L^*$	α
HAE	0.25	-3.53±0.14	41.73±0.12	-1.59±0.05	-3.55±0.11	41.95±0.09	-1.53±0.04
HAE	0.40	-3.45±0.16	41.86±0.11	-1.75±0.06	-4.18±0.27	42.73±0.24	-1.82±0.04
O3E	0.63	-3.04±0.15	41.59±0.10	-1.42±0.14	-3.36±0.16	41.97±0.10	-1.66±0.11
O3E	0.84	-3.71±0.21	42.17±0.11	-1.95±0.11	-3.66±0.22	42.41±0.13	-1.83±0.12
O2E	1.19	-2.81±0.25	41.99±0.15	-1.51±0.28	-2.90±0.09	42.43±0.06	-1.51±0.09
O2E	1.47	-2.88±0.30	42.10±0.15	-1.83±0.33	-2.74±0.10	42.48±0.06	-1.41±0.14

Note: ϕ^* is in units of Mpc^{-3} dex^{-1} and L^* is in units of erg s^{-1}.

Table 5. Same as Table4, but α is fixed to be -1.6 in fitting to the luminosity function.

		No correction for dust extinction			Corrected for dust extinction		
	redshift	$\log\phi^*$	$\log L^*$	α	$\log\phi^*$	$\log L^*$	α
HAE	0.25	-3.55±0.07	41.74±0.09	-1.6	-3.74±0.07	42.07±0.10	-1.6
HAE	0.40	-3.14±0.05	41.68±0.06	-1.6	-3.43±0.07	42.21±0.09	-1.6
O3E	0.63	-3.25±0.07	41.70±0.08	-1.6	-3.27±0.05	41.93±0.05	-1.6
O3E	0.84	-3.24±0.06	41.95±0.05	-1.6	-3.32±0.06	42.24±0.06	-1.6
O2E	1.19	-2.89±0.11	42.03±0.10	-1.6	-2.99±0.04	42.48±0.03	-1.6
O2E	1.47	-2.72±0.10	42.02±0.07	-1.6	-2.89±0.05	42.56±0.04	-1.6

Note: ϕ^* is in units of Mpc^{-3} dex^{-1} and L^* is in units of erg s^{-1}.

where i is for individual galaxies with $\log L \pm 0.5\Delta(\log L)$ (§4.2.1), V_{max} is the survey volume (§4.2.2) and f_c is detection completeness (§2.3.1). The detection completeness is taken into account based on both NB (proxy of emission-line flux) and BB (proxy of stellar continuum underlying the emission line) magnitudes (Figure 3).

Figures 14–16 show the observed luminosity functions for HAEs, O3Es, and O2Es at each redshift, i.e., dust extinction in emission line is not corrected yet. Because luminosity functions can be corrected for dust extinction in a few different ways, the observed luminosity functions are the simplest ones to compare with the results from the literature. The luminosity function is derived from galaxies in all of the fields surveyed. Note that we do not double count the galaxies in the overlapping regions between the UD-COSMOS and D-COSMOS fields to derive the luminosity functions. The luminosity functions in the individual UD and D fields are also shown with different colors in the figures, which is useful to indicate the field variance that illustrates how consistently the luminosity functions are derived for the individual fields. The sample variance is discussed in § 5.1. We fit a Schechter function (Schechter 1976) to the luminosity functions, where the Schechter function is:

$$\phi(L)dL = \phi^* \left(\frac{L}{L^*}\right)^{\alpha} \exp(-\frac{L}{L^*})\frac{dL}{L^*} , \quad (9)$$

or

$$\phi(L)d(\log L) = \phi^* \left(\frac{L}{L^*}\right)^{\alpha+1} \exp(-\frac{L}{L^*})\ \ln 10\ d(\log L) . \quad (10)$$

The Schechter parameters of the best-fit function are shown in Table 4. Table 5 also show the Schechter parameters of the best-fit function, but α is fixed to be -1.6 according to Sobral et al. (2013) and Sobral et al. (2015). The luminosity functions are well fit by the Schechter function. However, we notice that some luminosity functions show the excess of number density at the bright end from the best-fit Schechter function (e.g., O2Es in Figure 16), which is discussed in § 5.2.

For comparison with our results, luminosity functions from previous studies in wide fields are also plotted in Figures 14–16. Ly et al. (2007) conducted NB imaging with NB816 and NB921 on the Subaru/Suprime-Cam in the SDF of 0.24 deg^2. They selected NB816 and NB921 emitters with the observed EWs greater than 33 and 15 Å, respectively. The data are deeper than our HSC-SSP PDR1 data, but the area is much smaller than our survey. Drake et al. (2013) also conducted NB816 and NB921 imaging with Subaru/Suprime-Cam in the SXDS field of 0.63 deg^2. They applied the rest-frame EW cut of 100Å to their samples to derive luminosity functions. HiZELS conducted wider NB921 imaging with Subaru/Suprime-Cam in the COSMOS and UDS fields of $\sim$ 2 deg^2 (Sobral et al. 2013; Khostovan et al. 2015). They selected NB921 emitters with the rest-frame greater than 25 Å. The area covered by the previous studies are much smaller than HSC-SSP PDR1 data, because the Suprime-Cam only has one sevenths the FoV of HSC. However, these studies use the similar NB filters to those of HSC and thus the Hα, [OIII], and [OII] luminosity functions at the same redshifts are investigated.

Although our luminosity functions for all of HAEs, O3Es, and O2Es seem to be consistent with previous studies over the investigated luminosity ranges, the number density of our emitters may be slightly smaller than the previous studies in each luminosity bin. The small discrepancy can be caused by the relatively large EW cut in our samples: an observed EW of 48Å (56Å) for NB816 (NB921) emitters. Since the current NB data

of HSC-SSP is not so deep, we cannot give a strong constraint on the luminosity functions at less than $\sim 0.1L*$ ($0.3L*$) for O3Es (O2Es) at this time. On the other hand, the faint end of luminosity functions for HAEs reaches down to $\sim 0.01L*$.

Our luminosity functions for NB816 (NB921)-selected emission-line galaxies are based on 5.68 (16.2) deg^2 data, which is one of the widest NB imaging data sets. The number density of bright galaxies is low and survey volume for galaxies at lower redshifts is also not large, which suggests that the results for brighter galaxies at lower redshifts are more sensitive to the area of the field surveyed. Indeed, the bright end of our luminosity functions is determined by the emitters in the D fields. Thanks to the wide-field data, we can give a constraint on the luminosity functions up to the larger luminosity bins than investigated by the previous studies.

4.2.4 Intrinsic luminosity function

To derive the intrinsic luminosity functions for the emission-line galaxies, it is important that the luminosities are corrected for dust extinction. We estimate an amount of the dust extinction in the NB-measured emission-line fluxes using the Hα/Hβ line ratios of the SDSS analogs (Appendix 2). Based on stellar mass and observed luminosity of the targeted emission line (for example, [OII] for O2Es), we estimate the Balmer decrement for the individual galaxies. Then, assuming the Cardelli et al. (1989) extinction curve and the intrinsic Hα/Hβ ratio of 2.86 for Case B recombination under an electron temperature of $T_e = 10^4$ K and electron density of $n_e = 10^2$ cm^{-3} (Osterbrock 1989), the estimated Hα/Hβ ratio is converted to the magnitude of dust attenuation in the targeted line.

The previous studies have presented the typical dust extinction in emission line from a star-forming galaxy as a function of stellar mass, using the SDSS data (e.g., Gilbank et al. 2010; Garn & Best 2010). Although the dust extinction estimated by our method is comparable to the estimation by the previous studies, our method allows us to correct the luminosity of emission lines for dust extinction in the consistent way for HAEs, O3Es, and O2Es.

Figures 17–19 show the luminosity functions corrected for dust extinction for HAEs, O3Es, and O2Es at each redshift. The Schechter parameters of the best-fit function are provided in Tables 4–5. The luminosity functions from the previous studies are also plotted for the comparison. The method of the dust correction is different from ours, but our luminosity functions are consistent with the previous studies. The number density of our emitters may be slightly smaller than the previous studies at each luminosity bin, but that is likely due to the relatively large EW cut in our samples.

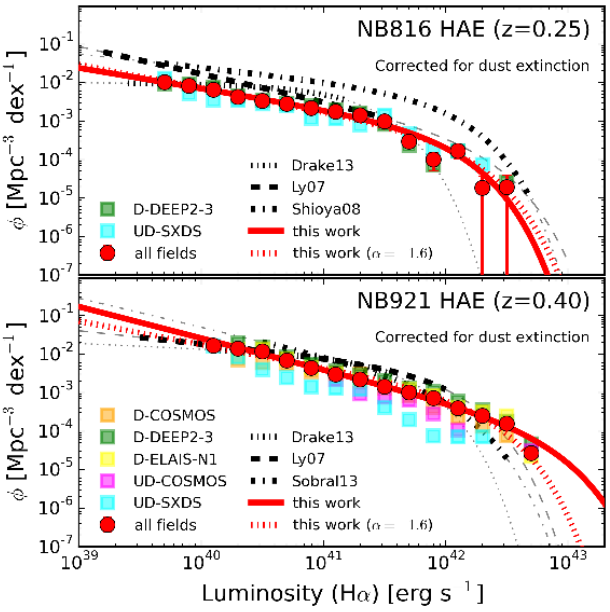

Fig. 17. The same as Figure 14, but the luminosities are corrected for dust extinction. The luminosity functions from the literature (Ly et al. 2007; Drake et al. 2013; Sobral et al. 2013; Shioya et al. 2008) are plotted for comparison.

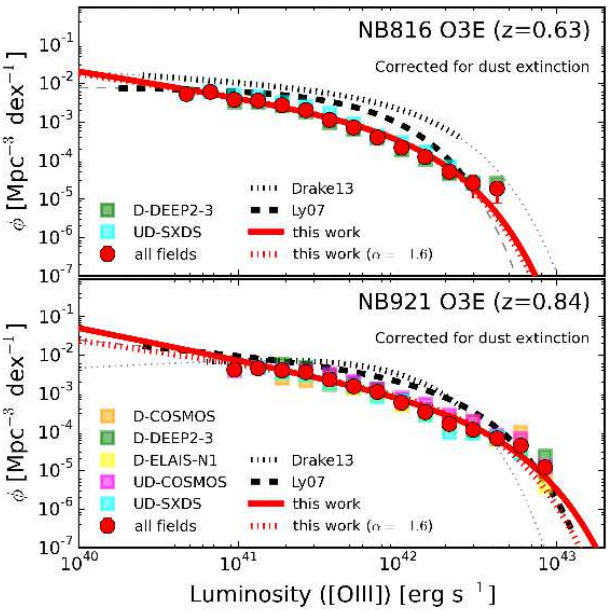

Fig. 18. The same as Figure 15, but the luminosities are corrected for dust extinction. The luminosity functions from the literature (Ly et al. 2007; Drake et al. 2013) are plotted for comparison.

5 Discussion

5.1 Sample variance

Cosmic variance is a non-negligible problem to properly understand representative properties of galaxy populations. Indeed, Figures 14–16 show that there is a scatter in the luminosity func-

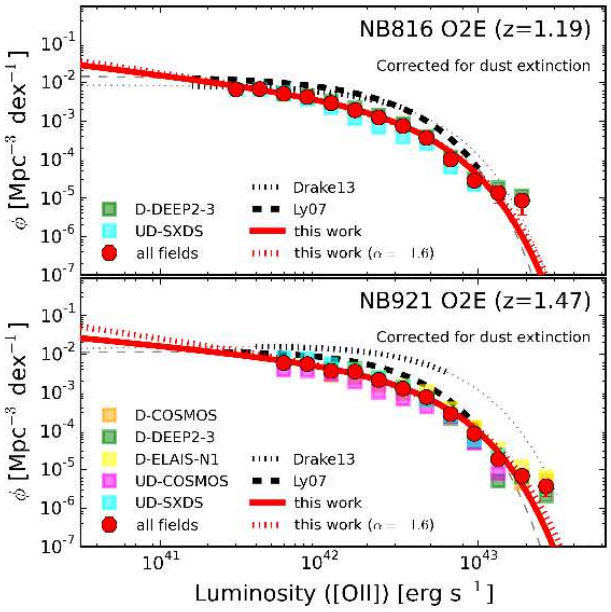

Fig. 19. The same as Figure 16, but the luminosities are corrected for dust extinction. The luminosity functions from the literature (Ly et al. 2007; Drake et al. 2013) are plotted for comparison.

tions for HAEs at $z = 0.40$ between the fields, although the other luminosity functions for HAEs at $z = 0.25$, O3Es and O2Es are mostly consistent between fields.

The typical survey volume for HAEs at $z \sim 0.40$ in the UD fields is $\sim 1 \times 10^5$ Mpc^3, which is a factor of $\sim 5-10$ smaller than the survey volume of the other fields. The luminosity functions for the HAEs at $z \sim 0.25$ in the two fields and the HAEs at $z \sim 0.40$ in the UD fields, all of which have a survey volume of $< 5 \times 10^5$ Mpc^3, are consistent with each other. Also, the luminosity functions for the other emission-line galaxies in larger survey volume are in agreement with each other between the fields irrespective of the UD and D fields.

The slight discrepancy in luminosity function for the HAEs at $z \sim 0.4$ is between the UD and D fields. Given the luminosity functions shown in Figure 14, the survey volume of $\sim 1 \times 10^5$ Mpc^3 in the UD fields implies that there can be at most several galaxies detected in the luminosity bins with $> 10^{42}$ erg s^{-1}. On the other hand, at $L \sim 2 \times 10^{41}$ erg s^{-1}, where the difference between the UD and D fields begins to become larger, there should be dozens of galaxies detected in the luminosity bins even in the UD fields. According to Trenti & Stiavelli (2008), we estimate the effect of cosmic variance in the luminosity function of HAEs at $z \sim 0.4$. The estimated uncertainty in the number of HAEs is $\sim$40%, which suggests that the dispersion in the number density of HAEs with $L > 2 \times 10^{41}$ can be explained by the cosmic variance. However, Figures 14 and 17 show that the number density of HAEs in the UD fields are systematically smaller than that in the D fields at any luminosity bins. This indicates that the two UD fields may be an underdense region of HAEs at $z \sim 0.4$.

Therefore, the comparison of the luminosity functions between the fields shows that the luminosity functions in the individual fields are consistent with each other and the survey volume of $> 5 \times 10^5$ Mpc^3 is essential at least to overcome the cosmic variance. Sobral et al. (2015) also reach the similar conclusion that a survey volume of $> 5 \times 10^5$ Mpc^3 is required to derive the luminosity functions with an error of less than 10% irrespective of sample variance.

5.2 Bright end of luminosity function

It is known that hard radiation from AGNs can contribute to emission lines from galaxies. The larger ionization energy required for [OIII] than [OII] and Hα implies that there is a possibility that the fraction of AGN contamination in O3Es is higher than HAEs and O2Es. However, contrary to the expectations, no strong excess of luminosity function is seen at the bright end for HAEs and O3Es (Figures 14 and 15), while a slight excess is seen in the luminosity functions for O2Es (Figure 16). Similar excess in bright end of luminosity function is reported by the previous studies (Matthee et al. 2017).

As mentioned in § 2.3.3, we limit the samples to galaxies fainter than 17.5 mag. Taking account of the EW cut as well that we apply in the selection of emission-line galaxies, we can miss most of NB816 (NB921) emitters with line fluxes larger than 5.5 (5.0) $\times$ 10^{-15} erg s^{-1} cm^{-1}. The fluxes corresponds to L/[erg s^{-1}] = 1.0×10^{42}, 9.3×10^{42}, and 4.4×10^{43} for NB816 HAEs, O3Es, and O2Es, and 2.9×10^{42}, 1.7×10^{43}, and 6.8×10^{43} for NB921 HAEs, O3Es, and O2Es, respectively. Therefore, the HSC-SSP PDR1 data are capable of selecting luminous emitters in the luminosity ranges investigated, although some emission-line galaxies at the bright end can be missed if more luminous galaxies tend to have a larger EW (e.g., Sobral et al. 2014). The limitation on the bright end confirms that there is no deviation of luminosity function from the Schechter function in HAEs and O3Es, while there is a slight deviation of O2E luminosity function from the Schechter function at the bright end.

Matthee et al. (2017) argue that the excess of the bright end of luminosity function is caused by AGNs and for HAEs at $z \sim$1.47 and 2.2 the fraction of X-ray sources in the HAEs monotonically increases with the Hα luminosity at $L(\mathrm{H}\alpha) > 10^{42.5}$ erg s^{-1} irrespective of redshift (see also Sobral et al. 2016). On the other hand, as described in §3.5, matching our samples of emission-line galaxies to the catalog of the Chandra X-ray sources in the COSMOS field (Marchesi et al. 2016) indicates that at most 0.1% of the emission-line galaxies are detected in X-ray as well. The fraction of O2Es with an X-ray counterpart is similar to that for HAEs and O3Es. Furthermore, since the X-ray counterpart of O2Es have the observed [OII] luminosity of $< 10^{42}$ erg s^{-1}, the O2Es with X-ray detection

do not have a large [OII] luminosity contributing to the bright end of the luminosity function. Indeed, the intrinsic luminosity functions corrected for dust extinction for not only O2Es but also HAEs and O3Es show no excess from the Schechter function at the bright end (Figures 17–19). There are few emission-line galaxies with the luminosities of $L > 10^{42.5}$ erg s^{-1}, which may cause the discrepancy between our results and those of Matthee et al. (2017). Therefore, we conclude that a strong excess at the bright end is not seen in our luminosity functions.

5.3 Stellar mass function

The stellar mass of galaxies is one of fundamental properties to characterize galaxies. There are many properties such as SFR, metallicity, dust extinction, and size that show a strong correlation with stellar mass. Since our samples of emission-line galaxies are based on the luminosity of nebular emissions which are indicators of SFR, they are SFR-limited samples to a first order approximation. Considering that there is a tight correlation between stellar mass and SFR in star-forming galaxies at each redshift (e.g., Speagle et al. 2014), it is expected that NB emission-line galaxy samples can contain star-forming galaxies with stellar mass down to a certain completeness limit. Therefore, it is interesting to investigate the stellar mass function of emission-line galaxies to better understand our samples.

We discuss for only HAEs hereafter in this section. This is because the stellar masses for HAEs are reliable, but those for O3Es and O2Es at $z > 0.8$ can be systematically overestimated (see §3.6 and Tanaka et al. 2017).

Figure 20 shows stellar mass function for HAEs. The stellar mass functions of HAEs at $z \sim 0.4$ show the difference in mass bins of $> 4 \times 10^{10}$ M$_\odot$ between the two fields of D-DEEP2-3 and D-ELAIS-N1 and the others. Figure 11 shows that the two fields have several galaxy clusters. Since the galaxy clusters are identified by red-sequence galaxies, the clustering of massive galaxies is reasonable.

We compare our stellar mass function with that of Sobral et al. (2014) (solid line) for HAEs at $z = 0.4$. While our stellar mass function is consistent with that of Sobral et al. (2014) at $M < 2 \times 10^9$ M$_\odot$, the number density of our HAEs is smaller than the Sobral et al. (2014) sample at $M > 2 \times 10^9$ M$_\odot$. As mentioned in § 3.1, the HSC-SSP PDR1 data can select the HAEs with the rest-frame EW larger than 40Å, while the sample of Sobral et al. (2014) includes the HAEs with the rest-frame EW larger than 25Å. Therefore, we miss the HAEs with small EWs that Sobral et al. (2014) can select. Since more massive galaxies tend to have a smaller EW on average (e.g., Sobral et al. 2014), the larger discrepancy between our stellar mass function and that of Sobral et al. (2014) at higher stellar masses is likely due to the difference of the limiting EW in the HAE selection.

Next, we compare our stellar mass function with those from star-forming galaxies at $z = 0.2$–0.5 (Ilbert et al. 2013; Muzzin et al. 2013; Davidzon et al. 2017). They construct the NIR-detected samples (i.e., stellar mass-limited samples in the first order approximation) in the COSMOS field covering 1.5–2 deg^2. Our stellar mass function is much lower than those from the literature and the discrepancy is larger in HAEs at $z = 0.25$ than HAEs at $z = 0.40$. This can be also caused again by the EW cut crucial for the NB emitter selection, as discussed above.

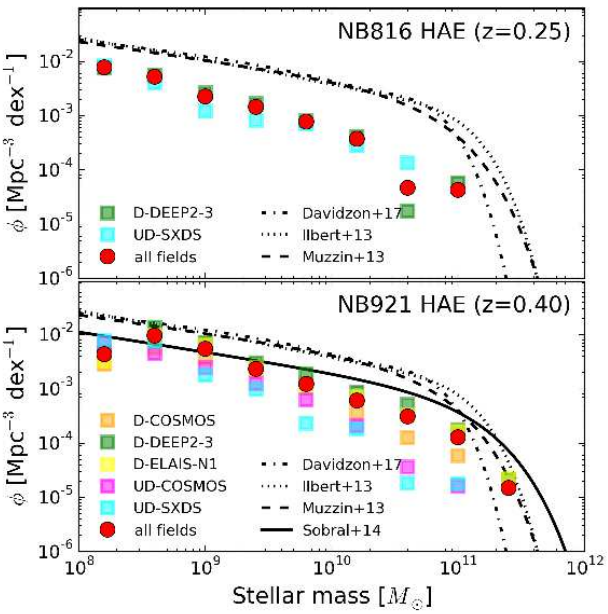

Fig. 20. Stellar mass function for HAEs. The luminosity functions from the literature are plotted for comparison: HAEs at $z = 0.4$ (Sobral et al. 2014) and star-forming galaxies at $z = 0.2$–0.5 (Ilbert et al. 2013; Muzzin et al. 2013; Davidzon et al. 2017)

Our samples cover the stellar mass range from $> 10^{11}$ M$_\odot$ down to $\sim 10^8$ M$_\odot$. The deeper data in both NB and BB are required to apply the smaller EW cut in the selection of emission-line and then make the more representative samples of star-forming galaxies.

6 Conclusions

The Subaru Strategic Program (SSP) with the Hyper Suprime-Cam (HSC) is an imaging survey with 300 nights over 5-6 years. The HSC-SSP provides us with widest and deepest data in five broadbands, g, r, i, z, and y, until the the Large Synoptic Survey Telescope (LSST) begins to operate, and another characteristic of the survey is that data from four narrowbands, NB387, NB816, NB921, and NB101 are available. The first public data release (PDR1) of the HSC-SSP is now publicly available, and consists of data taken over 61.5 nights.

We present initial results on emission-line galaxies at $z < 1.5$ selected with the data from two narrowband filters of

NB816 and NB921. The NB816 (NB921) data are available in the PDR1 over 5.7 (16) deg^2. The narrowband data enable us to select galaxies emitting Hα(λ6565Å) from $z \approx$ 0.25 and 0.40, [OIII](λ5008Å) from $z \approx 0.63$ and 0.84, and [OII]($\lambda\lambda 3727, 3730$Å) from $z \approx 1.19$ and 1.47. Main results that we present in this paper are the following.

1. This is one of the largest samples of emission-line galaxies at $z < 1.5$ ever constructed, which includes 1,193 (6,861) Hα emitters at $z \approx 0.24$ (0.40) down to the luminosities of $\log(\mathrm{L(H}\alpha)/[\mathrm{erg\ s^{-1}}]) \gtrsim 39.4$ (40.1), 2,228 (6,428) [OIII] emitters at $z \approx 0.63$ (0.84) down to the luminosities of $\log(\mathrm{L([OIII])/[erg\ s^{-1}}]) \gtrsim 40.4$ (40.8), and 5,861 (11,016) [OII] emitters at $z \approx 1.19$ (1.47) down to the luminosities of $\log(\mathrm{L([OII])/[erg\ s^{-1}}]) \gtrsim 41.1$ (41.4). The summary is shown in Table 3. The catalogs are available at the HSC-SSP website[4], after the paper is published.
2. The spatial distribution of the emitters shows large-scale structures over $\gtrsim$ 50 Mpc where galaxy clusters discovered by a red sequence cluster finding algorithm are embedded (Figures 11–13). This indicates that the samples include star-forming galaxies in various environments covering from the core of galaxy cluster to the void. The samples of emission-line galaxies are useful to investigate the environmental dependence of galaxy evolution at $z < 1.5$.
3. Luminosity functions of the emitters are investigated for Hα emitters at $z \sim 0.25$ and 0.40, [OIII] emitters at $z \sim$ 0.63 and 0.84, and [OII] emitters at $z \sim 1.19$ and 1.47 (Figures 14 – 16). The luminosity functions are mostly consistent with the previous studies at the luminosity ranges investigated. However, the number densities of our emitters may be slightly smaller than those of the previous studies. The slight discrepancy can be caused by the larger equivalent width cut in the selection of our emitters than the previous studies. The luminosity functions in each field surveyed by the HSC-SSP are consistent with each other, suggesting that more than 5×10^5 Mpc^3 is required at least to overcome the field variance.
4. Stellar mass functions are investigated for Hα emitters at $z \sim$ 0.25 and 0.40 (Figure 20), and then compared with the previous studies for Hα emitters at $z = 0.40$ and star-forming galaxies at $z =$ 0.2–0.5 from the stellar mass limited samples. The larger discrepancy is seen at higher stellar masses in Hα emitters at both $z = 0.25$ and $z = 0.40$, which suggests that there are star-forming galaxies with emission lines with small equivalent width that our NB imaging survey misses. The deeper data are essential to construct more representative samples of star-forming galaxies at the redshifts probed.

The HSC-SSP survey is ongoing. As the survey proceeds further, the coverage where NB data are available will be by a factor of 1.6 wider in the D fields and the depth of NB816 and NB921 is 0.5–0.6 (0.2–0.3) mag deeper in the UD (D) fields than those in the PDR1 data (Aihara et al. 2017a). The wider and deeper data allow us to survey less massive star-forming galaxies with a lower SFR at higher selection completeness and derive fainter end of luminosity function more reliably. We will update the catalogs of emission-line galaxies based on the upcoming data releases.

Acknowledgments

We thank the anonymous referee for providing constructive comments. MH acknowledges the financial support by JSPS Grant-in-Aid for Young Scientists (A) Grant Number JP26707006. This work is supported by World Premier International Research Center Initiative (WPI Initiative), MEXT, Japan, and KAKENHI (15H02064) Grant-in-Aid for Scientific Research (A) through Japan Society for the Promotion of Science (JSPS).

This work is based on data collected at Subaru Telescope, which is operated by the National Astronomical Observatory of Japan. The NB816 filter was supported by Ehime University and the NB921 filter was supported by KAKENHI (23244025) Grant-in-Aid for Scientific Research (A) through the JSPS.

The Hyper Suprime-Cam (HSC) collaboration includes the astronomical communities of Japan and Taiwan, and Princeton University. The HSC instrumentation and software were developed by the National Astronomical Observatory of Japan (NAOJ), the Kavli Institute for the Physics and Mathematics of the Universe (Kavli IPMU), the University of Tokyo, the High Energy Accelerator Research Organization (KEK), the Academia Sinica Institute for Astronomy and Astrophysics in Taiwan (ASIAA), and Princeton University. Funding was contributed by the FIRST program from Japanese Cabinet Office, the Ministry of Education, Culture, Sports, Science and Technology (MEXT), the Japan Society for the Promotion of Science (JSPS), Japan Science and Technology Agency (JST), the Toray Science Foundation, NAOJ, Kavli IPMU, KEK, ASIAA, and Princeton University. This paper makes use of software developed for the Large Synoptic Survey Telescope. We thank the LSST Project for making their code available as free software at [5]. The Pan-STARRS1 Surveys (PS1) have been made possible through contributions of the Institute for Astronomy, the University of Hawaii, the Pan-STARRS Project Office, the Max-Planck Society and its participating institutes, the Max Planck Institute for Astronomy, Heidelberg and the Max Planck Institute for Extraterrestrial Physics, Garching, The Johns Hopkins University, Durham University, the University of Edinburgh, Queens University Belfast, the Harvard-Smithsonian Center for Astrophysics, the Las Cumbres Observatory Global Telescope Network Incorporated, the National Central University of Taiwan, the Space Telescope Science Institute, the National Aeronautics and Space Administration under Grant No. NNX08AR22G issued through the Planetary Science Division of the NASA Science Mission Directorate, the National Science Foundation under Grant No. AST-1238877, the University of Maryland, and Eotvos Lorand University (ELTE) and the Los Alamos National Laboratory.

Appendix 1 Flags used for selection of NB-detected objects

hscPipe outputs a lot of flags showing reliability and measurement in source detection and photometry in the process of the data (Bosch et al. 2017). We apply the following flag cut to

[5] http://dm.lsst.org

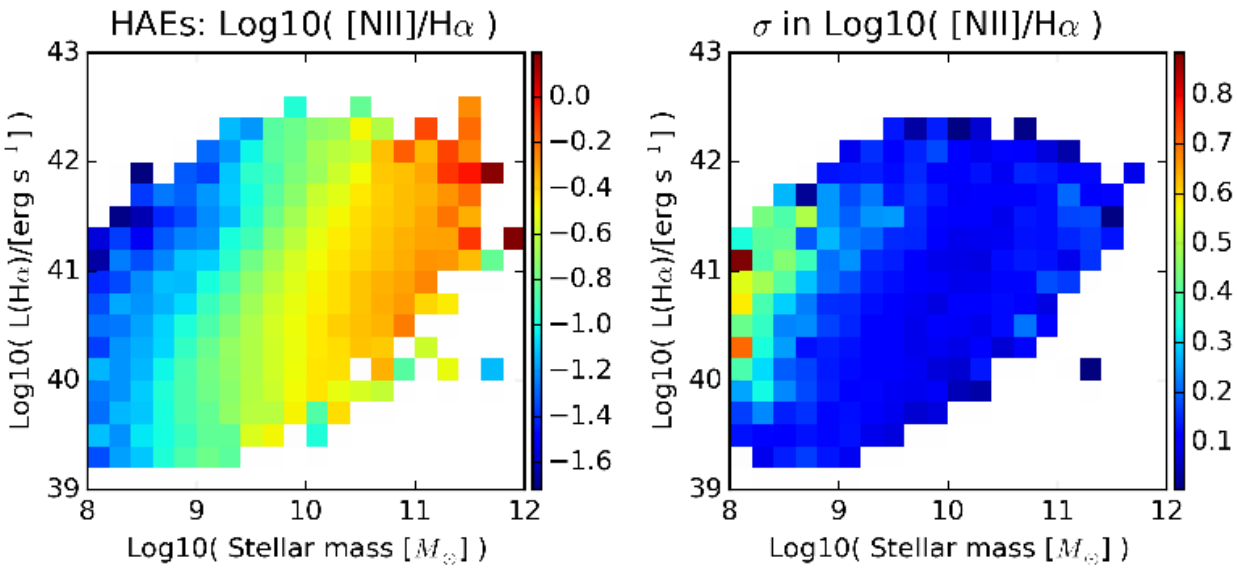

Fig. 21. Emission-line ratio of [NII]/Hα for the SDSS analogs of HAEs. The galaxies are selected from the SDSS spectroscopic catalog by applying the same EW cut as for the NB-selected HAEs. The left panel shows the [NII]/Hα ratio in a log scale in each bin, while the right panel shows the standard deviation of the line ratio in a log scale in each bin.

select NB-detected objects (refer to Bosch et al. 2017 for the meaning of the individual flags):

In NB816 or NB921

`detect_is_primary=True`,
`merge_peak=True`,
`flags_pixel_cr_center=False`,
`flags_pixel_saturated_center=False`,
`flags_pixel_bad=False`,
`flags_pixel_suspect_center=False`,
`flags_pixel_offimage=False`,
`flags_pixel_bright_object_center=False`,
`centroid_sdss_flags=False`,
`cmodel_flux_flags=False`, and
`detected_notjunk=True`.

In i (z)-band for NB816 (NB921)-detected objects

`flags_pixel_cr_center=False`,
`flags_pixel_saturated_center=False`,
`flags_pixel_bad=False`,
`flags_pixel_suspect_center=False`, and
`flags_pixel_offimage=False`.

In all BBs

`flags_pixel_bright_object_center=False`.

Appendix 2 Emission-line ratios for the SDSS analogs of NB emitters

Since the [NII] doublet ($\lambda\lambda$6549.84,6585.23Å) is close to Hα (λ6564.61Å) line, all of the emission lines can enter the NB filter simultaneously. Also, emission-line fluxes can suffer dust extinction. To derive intrinsic luminosity of a specific emission line, a correction for the neighbor lines and the dust extinction is required. The SDSS data allow us to estimate such impact on the emission-line fluxes measured from the NB and BB photometry by selecting analogs of NB emission-line galaxies and then investigating the line ratios of emission lines.

The spectroscopic catalogs are extracted from the MPA-JHU release of spectrum measurements for the SDSS Data Release 7 (DR7) [6] (Kauffmann et al. 2003; Salim et al. 2007; Abazajian et al. 2009). To select the analogs of NB-selected emission-line galaxies, we apply the same EW cut as for the NB selection. We then investigate the various line flux ratio as a function of the observed emission-line luminosity and stellar mass.

Figure 21 shows the [NII]/Hα ratios for the analogs of HAEs as a function of the Hα luminosity and stellar mass. The ratios are used to correct the fluxes measured from the HSC-SSP data for the contribution of [NII]. Figure 22 is the same as Figure 21, but for the Hα/Hβ ratios, i.e., Balmer decrement for the analogs of HAEs, O3Es and O2Es. This is used for the correction of dust extinction. Figures 21 – 22 also show the standard deviation of the line ratio in each bin to infer an accuracy of the

[6] http://www.mpa-garching.mpg.de/SDSS/DR7/

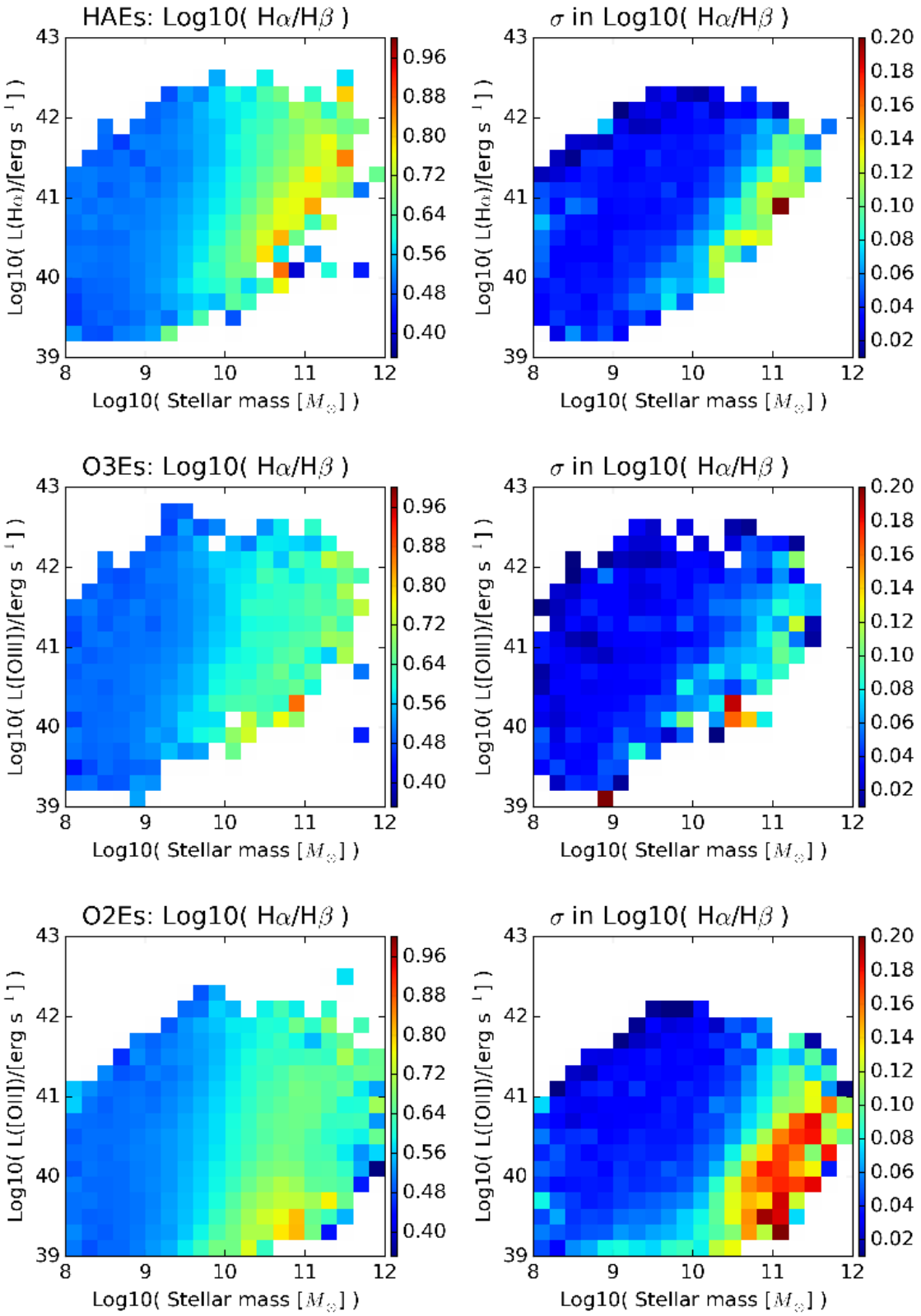

Fig. 22. The same as Figure 21, but for the line ratio of Hα/Hβ. The line ratios for the SDSS analogs of HAEs, O3Es, and O2Es are shown in top, middle, and bottom panels, respectively.

determination of the line ratios based on the stellar mass and the luminosity of the targeted emission line.

References

Abazajian, K. N., et al. 2009, ApJS, 182, 543

Aihara, H., et al. 2017a, arXiv: 1702.08449 (PDR1 paper)

—. 2017b, arXiv: 1704.05858 (Survey design paper)

Alam, S., et al. 2015, ApJS, 219, 12

An, F. X., et al. 2014, ApJ, 784, 152

Atek, H., et al. 2010, ApJ, 723, 104

Axelrod, T., Kantor, J., Lupton, R. H., & Pierfederici, F. 2010, in Proc. SPIE, Vol. 7740, Software and Cyberinfrastructure for Astronomy, 774015

Bacon, R., et al. 2015, A&A, 575, A75

Bayliss, K. D., McMahon, R. G., Venemans, B. P., Ryan-Weber, E. V., & Lewis, J. R. 2011, MNRAS, 413, 2883

Behroozi, P. S., Conroy, C., & Wechsler, R. H. 2010, ApJ, 717, 379

Best, P., et al. 2013, in Astrophysics and Space Science Proceedings, Vol. 37, Thirty Years of Astronomical Discovery with UKIRT, ed. A. Adamson, J. Davies, & I. Robson, 235

Bina, D., et al. 2016, A&A, 590, A14

Bosch, J., et al. 2017, arXiv: 1705.06766

Bradshaw, E. J., et al. 2013, MNRAS, 433, 194

Brammer, G. B., van Dokkum, P. G., Illingworth, G. D., Bouwens, R. J., Labbé, I., Franx, M., Momcheva, I., & Oesch, P. A. 2013, ApJL, 765, L2

Brammer, G. B., et al. 2012, ApJS, 200, 13

Brodwin, M., et al. 2013, ApJ, 779, 138

Bruzual, G., & Charlot, S. 2003, MNRAS, 344, 1000

Bunker, A. J., Warren, S. J., Hewett, P. C., & Clements, D. L. 1995, MNRAS, 273, 513

Calhau, J., Sobral, D., Stroe, A., Best, P., Smail, I., Lehmer, B., Harrison, C., & Thomson, A. 2017, MNRAS, 464, 303

Calzetti, D., Armus, L., Bohlin, R. C., Kinney, A. L., Koornneef, J., & Storchi-Bergmann, T. 2000, ApJ, 533, 682

Capak, P., et al. 2007, ApJS, 172, 99

Cardelli, J. A., Clayton, G. C., & Mathis, J. S. 1989, ApJ, 345, 245

Chabrier, G. 2003, PASP, 115, 763

Ciardullo, R., et al. 2013, ApJ, 769, 83

Civano, F., et al. 2016, ApJ, 819, 62

Coil, A. L., et al. 2011, ApJ, 741, 8

Colbert, J. W., et al. 2013, ApJ, 779, 34

Comparat, J., et al. 2015, A&A, 575, A40

—. 2016, MNRAS, 461, 1076

Cool, R. J., et al. 2013, ApJ, 767, 118

Coupon, J., Czakon, N., Bosch, J., Komiyama, Y., Medezinski, E., Miyazaki, S., & Oguri, M. 2017, arXiv: 1705.00622

Daddi, E., et al. 2007, ApJ, 670, 156

Dale, D. A., et al. 2010, ApJL, 712, L189

Darvish, B., Mobasher, B., Martin, D. C., Sobral, D., Scoville, N., Stroe, A., Hemmati, S., & Kartaltepe, J. 2017, ApJ, 837, 16

Darvish, B., Mobasher, B., Sobral, D., Rettura, A., Scoville, N., Faisst, A., & Capak, P. 2016, ApJ, 825, 113

Darvish, B., Mobasher, B., Sobral, D., Scoville, N., & Aragon-Calvo, M. 2015, ApJ, 805, 121

Darvish, B., Sobral, D., Mobasher, B., Scoville, N. Z., Best, P., Sales, L. V., & Smail, I. 2014, ApJ, 796, 51

Davidzon, I., et al. 2017, arXiv: 1701.02734

Davis, M., et al. 2003, in Proc. SPIE, Vol. 4834, Discoveries and Research Prospects from 6- to 10-Meter-Class Telescopes II, ed. P. Guhathakurta, 161–172

Doherty, M., Bunker, A., Sharp, R., Dalton, G., Parry, I., & Lewis, I. 2006, MNRAS, 370, 331

Drake, A. B., et al. 2013, MNRAS, 433, 796

Drinkwater, M. J., et al. 2010, MNRAS, 401, 1429

Elbaz, D., et al. 2007, A&A, 468, 33

Fujita, S. S., et al. 2003, ApJL, 586, L115

Garilli, B., et al. 2014, A&A, 562, A23

Garn, T., & Best, P. N. 2010, MNRAS, 409, 421

Garn, T., et al. 2010, MNRAS, 402, 2017

Gilbank, D. G., Baldry, I. K., Balogh, M. L., Glazebrook, K., & Bower, R. G. 2010, MNRAS, 405, 2594

Hayashi, M., Kodama, T., Koyama, Y., Tanaka, I., Shimasaku, K., & Okamura, S. 2010, MNRAS, 402, 1980

Hayashi, M., Kodama, T., Tanaka, I., Shimakawa, R., Koyama, Y., Tadaki, K.-i., Suzuki, T. L., & Yamamoto, M. 2016, ApJL, 826, L28

Hayashi, M., Sobral, D., Best, P. N., Smail, I., & Kodama, T. 2013, MNRAS, 430, 1042

Hayashi, M., et al. 2015, PASJ, 67, 80

Hilton, M., et al. 2010, ApJ, 718, 133

Hopkins, A. M., & Beacom, J. F. 2006, ApJ, 651, 142

Hsieh, B. C., & Yee, H. K. C. 2014, ApJ, 792, 102

Huang, S., et al. 2017, arXiv: 1705.01599

Ilbert, O., et al. 2013, A&A, 556, A55

Ishiyama, T., Enoki, M., Kobayashi, M. A. R., Makiya, R., Nagashima, M., & Oogi, T. 2015, PASJ, 67, 61

Ivezic, Z., et al. 2008, arXiv: 0805.2366

Jurić, M., et al. 2015, arXiv: 1512.07914

Kashikawa, N., et al. 2004, PASJ, 56, 1011

Kashino, D., et al. 2013, ApJL, 777, L8

Kauffmann, G., et al. 2003, MNRAS, 341, 33

Kawanomoto et al. 2017, in preparation

Kennicutt, Jr., R. C. 1998, ARA&A, 36, 189

Kewley, L. J., Geller, M. J., & Jansen, R. A. 2004, AJ, 127, 2002

Khostovan, A. A., Sobral, D., Mobasher, B., Best, P. N., Smail, I., Stott, J. P., Hemmati, S., & Nayyeri, H. 2015, MNRAS, 452, 3948

Koyama, Y., Kodama, T., Nakata, F., Shimasaku, K., & Okamura, S. 2011, ApJ, 734, 66

Koyama, Y., Kodama, T., Shimasaku, K., Hayashi, M., Okamura, S., Tanaka, I., & Tokoku, C. 2010, MNRAS, 403, 1611

Koyama, Y., Kodama, T., Tadaki, K.-i., Hayashi, M., Tanaka, I., & Shimakawa, R. 2014, ApJ, 789, 18

Koyama, Y., et al. 2013, MNRAS, 434, 423

—. 2017, arXiv: 1704.05979

Kuutma, T., Tamm, A., & Tempel, E. 2017, A&A, 600, L6

Laigle, C., et al. 2016, ApJS, 224, 24

—. 2017, arXiv: 1702.08810

Le Fèvre, O., et al. 2013, A&A, 559, A14

Lee, J. C., et al. 2012, PASP, 124, 782

Lilly, S. J., et al. 2009, ApJS, 184, 218

Ly, C., Lee, J. C., Dale, D. A., Momcheva, I., Salim, S., Staudaher, S., Moore, C. A., & Finn, R. 2011, ApJ, 726, 109

Ly, C., et al. 2007, ApJ, 657, 738

Madau, P., & Dickinson, M. 2014, ARA&A, 52, 415

Magnier, E. A., et al. 2013, ApJS, 205, 20
Malavasi, N., et al. 2017, MNRAS, 465, 3817
Marchesi, S., et al. 2016, ApJ, 817, 34
Matthee, J., Sobral, D., Best, P., Smail, I., Bian, F., Darvish, B., Röttgering, H., & Fan, X. 2017, arXiv: 1702.04721
McLure, R. J., et al. 2013, MNRAS, 428, 1088
Mehta, V., et al. 2015, ApJ, 811, 141
Meillier, C., Chatelain, F., Michel, O., Bacon, R., Piqueras, L., Bacher, R., & Ayasso, H. 2016, A&A, 588, A140
Miyazaki, S., et al. 2012, in Proc. SPIE, Vol. 8446, Ground-based and Airborne Instrumentation for Astronomy IV, 84460Z
Miyazaki et al. 2017, PASJ, accepted for a HSC special issue of PASJ
Momcheva, I. G., et al. 2016, ApJS, 225, 27
Moorwood, A. F. M., van der Werf, P. P., Cuby, J. G., & Oliva, E. 2000, A&A, 362, 9
Morris, A. M., et al. 2015, AJ, 149, 178
Moustakas, J., Kennicutt, Jr., R. C., & Tremonti, C. A. 2006, ApJ, 642, 775
Muzzin, A., et al. 2013, ApJ, 777, 18
Nelson, E. J., et al. 2012, ApJL, 747, L28
—. 2016, ApJ, 828, 27
Newman, J. A., et al. 2013, ApJS, 208, 5
Noeske, K. G., et al. 2007, ApJL, 660, L43
Oguri, M. 2014, MNRAS, 444, 147
Oguri, M., et al. 2017, arXiv: 1701.00818
Oke, J. B., & Gunn, J. E. 1983, ApJ, 266, 713
Osterbrock, D. E. 1989, Astrophysics of gaseous nebulae and active galactic nuclei
Oteo, I., Sobral, D., Ivison, R. J., Smail, I., Best, P. N., Cepa, J., & Pérez-García, A. M. 2015, MNRAS, 452, 2018
Ouchi, M., et al. 2008, ApJS, 176, 301
—. 2010, ApJ, 723, 869
Pirzkal, N., et al. 2013, ApJ, 772, 48
Ramraj, R., Gilbank, D. G., Blyth, S.-L., Skelton, R. E., Glazebrook, K., Bower, R. G., & Balogh, M. L. 2017, MNRAS, 466, 3143
Rodighiero, G., et al. 2011, ApJL, 739, L40
Salim, S., et al. 2007, ApJS, 173, 267
Schaye, J., et al. 2015, MNRAS, 446, 521
Schechter, P. 1976, ApJ, 203, 297
Schlafly, E. F., et al. 2012, ApJ, 756, 158
Shioya, Y., et al. 2008, ApJS, 175, 128
Shivaei, I., et al. 2015, ApJ, 815, 98
Silverman, J. D., et al. 2015, ApJS, 220, 12
Skelton, R. E., et al. 2014, ApJS, 214, 24
Sobral, D., Best, P. N., Matsuda, Y., Smail, I., Geach, J. E., & Cirasuolo, M. 2012, MNRAS, 420, 1926
Sobral, D., Best, P. N., Smail, I., Geach, J. E., Cirasuolo, M., Garn, T., & Dalton, G. B. 2011, MNRAS, 411, 675
Sobral, D., Best, P. N., Smail, I., Mobasher, B., Stott, J., & Nisbet, D. 2014, MNRAS, 437, 3516
Sobral, D., Kohn, S. A., Best, P. N., Smail, I., Harrison, C. M., Stott, J., Calhau, J., & Matthee, J. 2016, MNRAS, 457, 1739
Sobral, D., Smail, I., Best, P. N., Geach, J. E., Matsuda, Y., Stott, J. P., Cirasuolo, M., & Kurk, J. 2013, MNRAS, 428, 1128
Sobral, D., et al. 2015, MNRAS, 451, 2303
Speagle, J. S., Steinhardt, C. L., Capak, P. L., & Silverman, J. D. 2014, ApJS, 214, 15
Straughn, A. N., et al. 2011, AJ, 141, 14
Stroe, A., & Sobral, D. 2015, MNRAS, 453, 242
Stroe, A., Sobral, D., Paulino-Afonso, A., Alegre, L., Calhau, J., Santos, S., & van Weeren, R. 2017, MNRAS, 465, 2916
Stroe, A., Sobral, D., Röttgering, H. J. A., & van Weeren, R. J. 2014, MNRAS, 438, 1377
Stroe, A., et al. 2015, MNRAS, 450, 646
Suzuki, T. L., et al. 2016, MNRAS, 462, 181
Swinbank, A. M., et al. 2017, MNRAS, 467, 3140
Takata et al. 2017, in preparation
Tanaka, M. 2015, ApJ, 801, 20
Tanaka, M., et al. 2017, arXiv: 1704.05988
Thompson, D., Mannucci, F., & Beckwith, S. V. W. 1996, AJ, 112, 1794
Tomczak, A. R., et al. 2016, ApJ, 817, 118
Tonry, J. L., et al. 2012, ApJ, 750, 99
Trenti, M., & Stiavelli, M. 2008, ApJ, 676, 767
van der Wel, A., et al. 2011, ApJ, 742, 111
van der Werf, P. P., Moorwood, A. F. M., & Bremer, M. N. 2000, A&A, 362, 509
van Dokkum, P. G., et al. 2011, ApJL, 743, L15
Villar, V., Gallego, J., Pérez-González, P. G., Pascual, S., Noeske, K., Koo, D. C., Barro, G., & Zamorano, J. 2008, ApJ, 677, 169
Vogelsberger, M., et al. 2014, MNRAS, 444, 1518
Whitaker, K. E., et al. 2014, ApJ, 795, 104
Yuma, S., Ouchi, M., Drake, A. B., Fujimoto, S., Kojima, T., & Sugahara, Y. 2017, ApJ, 841, 93
Yuma, S., et al. 2013, ApJ, 779, 53